Phenotype Heterogeneity Warrants Trizonal Feedback between Intracellular Contractility and Extracellular stiffening

M. E. Torki[1], Z. Chen[2*], F. Liu[2]

[1] *School of Engineering and Applied Science, University of Pennsylvania, Philadelphia, PA 19104, USA*

[2] *Brigham and Women's Hospital and Harvard Medical School, Boston, MA 02115*

Abstract

The two-way feedback loop between intracellular actomyosin contractility and extracellular matrix (ECM) strain stiffening along with fiber realignment drives the phenotype of cancer cell invasion. The latter is construed via cell elongation, protrusion and contractile stiffening. Accordingly, the combined impact of ECM strain stiffening and cell contractility plays a pivotal role in heterogeneity of cell populations and their invasiveness (reflected in cell elongation and normalized PercevalHR ratio) in response to ECM stiffness increase. Existing constitutive models fail to predict multimodal cell shapes based on their motility levels. Hence, this article suggests a free energy-based trizonal nonlinear model of cell durotaxis that incorporates all factors affecting the two-way feedback between the cell and ECM. As such, the proposed model is primarily invoked for evaluation of steady-state optimal cell shape and contractility in terms of ECM stiffness, contractility density, stress anisotropy (polarization), membrane-cortical tension, and integrin contribution by employing total free energy minimization. The trizonal model is further suggestive of a lowly motile zone with limited cell invasiveness as being insensitive to ECM stiffness, a highly motile zone corresponding to highly invasive, *i.e.* elongated cells heavily influenced by stiffness, and a mesoregion of stiffness corresponding to two possible cell states. The lower end to the latter represents a critical stiffness required for intercellular deadhesion and initiation of maximal cell invasion. Consequently, a statistical representation of the model can both regenerate and predict the multimodal dispersion of cell shapes in human functional tissue assays.

Key Words: Cell invasion | Cell contractility | Matrix stiffness | Collagen density | Rho pathway.

*Corresponding author. Email: zchen33@bwh.harvard.edu

Significance

ECM stiffening is a central feature for prompting metastatic phenotypes. Two-way feedback between cell contractility and ECM stiffening is enormously affected by the cell motility level. Distinct cell shapes have been earlier manifested under the influence of cell contractility and adhesion for epithelial tissue morphogenesis during embryo development [1–3]. Recent outcomes unveil similar existence of distinct mesenchymal cell populations, with assorted elongations in terms of motility levels [4–7]. Accordingly, lowly and highly motile cells prove insensitive and highly sensitive to ECM stiffness, respectively [7]. Correspondingly, cells belonging to one assay can adopt more than one predominant shape in a finite range of ECM stiffnesses, delivering a multi-modal histogram. Existing chemo-mechanical models, however, cannot fully distinguish among different cell populations based on their motility levels. Likewise, they fail to physically replicate recently observed biphasic cell response vs. ECM stiffness, which is justifiable via the same physical concept.

1 Introduction

Chemo-mechanically interacting intracellular and extracellular cues within the cell-matrix microenvironment are primary origins of epithelial-to-mesenchymal transition (EMT) triggering metastatic cell migration. That is, cytoskeletal tension, actomyosin contractility, cell stiffness and extracellular matrix (ECM) fiber realignment are tightly correlated in malignant phenotypes [8–12]. The outward reflection of this multifaceted correlation is measurable and observable, respectively through cell elongation and/or protrusion as well as cell contractility evaluated via the normalized PercevalHR ratio [12–16]. ECM strain stiffening and trans-membrane adhesion between the actin cytoskeleton and ECM are two salient factors affecting the prevailing cell shape. The latter is provided prevalently by integrins and less commonly through other adhesion receptors such as cadherins, selectins, and

immunoglobulin-like cell adhesion molecules (Ig-CAM) [17]. Integrins act through focal adhesions that anchor the cell to ECM and transmit traction forces generated through actomyosin contractility [18–22].

Depending on the composition and linkage between their subunits, cell motility and invasion under the influence of integrins can be immensely enhanced [23], mitigated [24] or both [25–29]. In essence, high integrin expressions have a demonstrated capability of mediating multifold increase in contractility (reported for $\alpha 5\beta 1$ for instance [22, 26–29]) as well as significant reduction of cell invasiveness following addition of myosin light chain kinase inhibitor (ML-7) while the latter bears no influence on low integrin expressions [22]. The former factor, however, is still in premature exploration. Indeed, a full-range effect of ECM stiffness and its relevant parameters such as collagen density has remained elusive until recent years, hence making some subtle controversy discernible within the relevant literature. Earlier work suggest elevation of cell invasion upon observable increase in ECM stiffness in conjunction with matrix fiber alignment and increased collagen density [30–34]. Accordingly, the term "durotaxis" conventionally refers to migration of cells from a more compliant to a stiffer matrix [33, 35–37]. More recent findings, however, are indicative of biphasic rather than monotonically increasing cell motility, elongation and invasiveness upon increasing of the collagen matrix stiffness and/or collagen density [38–40]. As such, malignant phenotypes admittedly rely on generally stiff rather than soft matrices for metastasis due to their intensified realignment capability. Nevertheless, beyond an intermediate range of ECM stiffness inducing maximum motility, elongation and invasiveness, cells cannot intrude into tightly cross-linked pores any further, thus cell elongation and actomyosin contractility being reduced. Analogously, the latter contrast is conspicuous in aged skin fibroblasts as opposed to their young counterparts. That is, realignment of aged fibroblasts in stiff matrices promotes cell invasion whereas young fibroblasts compose a dense, isotropic matrix consistent with the so-called *basket weave* pattern [39, 41–43].

Metastatic cell migration is a highly anisotropic phenomenon [44]. The anisotropic nature of metastasis is by and large rooted in matrix fiber realignment [45–47] or stress polarization [16, 48–50]. While the former is self-evident, understanding the latter had been overlooked until quite recent times, hence still far from being exhaustive. The effect of polarization in the first principal stress on cell contractility has been phenomenologically observed through tissue sculpting in the interest of more intensive tissue alignment [50]. The complete physical process underlying such correlation, however, cannot be fully grasped unless by cell culture in 3D collagen environments. The observed two-way feedback between cell protrusion and matrix alignment gives rise to a self-reinforcing mechanism involving interactive extension and retraction of cell protrusions [16]. As such, pre-aligned matrix fibers trigger alignment within cell protrusions which, in turn, leads to collagen fiber realignment. Realigned collagen fibers would ultimately stabilize the directions of protrusions by retracting their extension in lateral directions. Correepondingly, actomyosin contractility is primarily promoted by stress anisotropy rather than its magnitude (normally represented with mean stress σ_{m}) [16, 49, 50]. For modeling purposes, Shenoy and coworkers have recently approached this problem by mere addition of a linear term appearing as a factor of the first principal stress such as $\alpha_{\mathrm{a}}\sigma_1$ to the total expression of mean contractility ρ_{m}, with α_{a} restricted as function of the ratio between the largest and smallest positive (tensile) principal stresses σ_1/σ_2 [16, 49, 50]. While well-motivated and partly consistent with experiment, such modeling has limited predictive capability from various perspectives. However, a full dissection of the limitations to such approach cannot be achieved unless by its formulation from first principles, *i.e.* by superposition of $\alpha_{\mathrm{a}}\sigma_1$ to the free energy with α_{a} left as an adjustable parameter (see SI Appendix, Section 1.1). Thereupon, the linear model can defectively capture the biphasic cell shape in terms of matrix stiffness only through a first-order transition from spherical to elongated shapes. Such linear transition is both non-physical and limited to extremely soft matrices. In particular, the intermediate ECM stiffness range delivering maximal contractility and elongation should physically vary with the chemo-mechanical coupling rooted in actomyosin motors and stress-dependent signalling pathways, something on which the linear model has no parametric control.

Here, we introduce a bistable trizonal nonlinear constitutive model, similar in bistable behavior to that proposed by Hannezo *et al.* [3] for epithelial cells, for migration of mesenchymal cells inside 3D matrix environments. The proposed model couples the distinct effects imparted by the cell and ECM through parametrized ECM stiffness and fiber alignment, contractility density, stress polarization, membrane stretching, and integrin contribution on the cell's adopted shape at steady state. The approach to this end solidifies into a minimized total cell free energy with respect to strain and contractility as well as cell body aspect ratio. The former minimization is carried out a' priori, expressing stress and contractility vs. strains whereas the latter minimization is executed a posteriori to predict the optimal cell shape primarily in terms of ECM stiffness. The bistable nature of the model yields three zones of contractility and optimal cell shape vs. ECM stiffness: (*i*) soft ECM zone characterized with low contractility and nearly spherical predominant cell shape, the two appearing insensitive to ECM stiff-

ness; (*ii*) medium-stiffness ECM zone overlapping two possible solutions, the lower branch predicting nearly-spherical cell shape and low contractility, and the upper branch predicting elongated (*i.e.* invasive) cell shape and high contractility; (*iii*) high-stiffness ECM zone characterized with high contractility and cell elongation. The lower end to the intermediate stiffness zone would deliver an estimate of a critical stiffness corresponding to maximal cell invasiveness, and its associated maximal aspect ratio. Such stiffness is physically required for intercellular deadhesion and initiation of maximal cell invasion. By employment of a compound machine-learning algorithm, the constitutive model is further implementable numerically on spheroidal cells embedded in a 3D fibrous matrix. The corresponding parametric calculations are then swept through the cell body aspect ratio as well as its contractility density whereby optimal parameter sets are extracted to replicate multimodal cell distribution. The distinct and combined effects of collagen stiffening, actomyosin and integrin inhibition are considered. Potential applications are multifold: from predicting cancer-induced tissue impairment and cachexia, inflammatory and oxidative muscle injury to assessment analysis of theraputic methods for reversal of such processes including Blebbistatin treatment of mesenchymal or epithelial cell cultures, HAPLN1 treatment of aged fibroblasts, myosin light-chain kinase inhibition, *etc.*

2 Model Derivation

2.1 Stress-induced signaling drives cell contractility, ATP consumption

The chemo-mechanical process that leads to shape transition in cells is reflected in generation of contractile forces, which originate from bonding betwee myosin motors and actin filaments [51–53]. Prior to being detached from actin filaments, myosin motors consume ATP whereby chemical energy released from ATP hydrolysis is converted into mechanical work. In a sufficiently stiff extracellular matrix (ECM), intracellular contraction generates tensile forces in the matrix, significant enough to generate feedback with the cell through stress-sensitive signaling pathways (*e.g.*, Rho-ROCK, Ca2+) [38, 51, 54]. Thereupon, continued binding of myosin motors and increasing contractile forces (through ATP consumption) would be promoted (Fig. 1a). Each cycle of contractile force generation lasts within the order of milliseconds. In order for the cell to remain contractile over longer time scales, the cycles of binding, force generation and unbinding must operate continuously so ATP is continuously consumed [55–58].

We focus our attention on one-dimensional variation first. Denoting the binding and unbinding time rates by $J_{\rm on} > 0$ and $J_{\rm off} < 0$, the time rate of changing motor density, alias *contractility*, can be written as

$$\dot{\rho} = J_{\rm on} + J_{\rm off} \tag{1}$$

To ensure the positivity of energy dissipation rate, the following forms are adopted for $J_{\rm on}$ and $J_{\rm off}$:

$$J_{\rm on} = -k_{\rm on}\left(\frac{\partial U}{\partial \rho} - \Delta G\right) \quad , \quad J_{\rm off} = -k_{\rm off}\left(\frac{\partial U}{\partial \rho}\right) \tag{2}$$

with $k_{\rm on} > 0$ and $k_{\rm off} < 0$ being kinetic parameters for binding and unbinding rates, and ΔG is a scale factor representing energy realesed through ATP hydrolyzation [61,77]. The steady state entails $\dot{\rho} = 0$, hence writing

$$\frac{\partial U}{\partial \rho} = \kappa \Delta G \tag{3}$$

where $\kappa = \frac{k_{\rm on}}{k_{\rm off}+k_{\rm on}}$.

The complete cycle of binding and unbinding consists mainly of the binding/unbinding of individual myosin motors (in milliseconds) and phosphorylation of myosin motors (binding enabler), which is regulated by stress through signaling pathways [55–58]. To capture the latter effect, $k_{\rm on}$ should be set as a function of the external stress σ. In existing linear models of cell durotaxis, myosin motors are taken to detach from the cytoskeleton immediately after the force generation cycle, thereby giving rise to a significantly higher unbinding probability. Accordingly, $k_{\rm off} >> k_{\rm on}$ and $k_{\rm off}$ is normally regarded constant. Such restriction, however, holds only under the circumstance of a large ATP resource, which proves overly restrictive under highly heterogeneous motor densities. Rather, highly motile cell shape transition under heterogeneous motility cannot be duly captured unless the binding rate is maintained above the unbinding rate, *i.e.* $k_{\rm on} = (\alpha\sigma)^p\, k_{\rm off}$, with α admitting a dimension of L^2/F. Such correlation captures the highly anisotropic nature of signaling pathways between cell and ECM. On the other hand, heterogeneity within the cell motility level at a given quiescent contractility level, *i.e.* at fixed contractile density ρ_0, calls for consideration of a fraction of the steady-state unbinding rate, here denoted with a constant parameter such as c. Altogether, the following mathematical form proves true to both spirits:

$$\kappa\left(\sigma\right) = \frac{\left(\alpha\sigma\right)^p}{1 + c\left(\alpha\sigma\right)^p} \tag{4}$$

with (p, c) being nondimensional parameters. Note that $p \geqslant 1$ and $0 \leqslant c \leqslant 1$, whereby the linear feedback model would be retrieved with $p = 1$ and $c = 0$. By virtue of Eq. (4), increases in the principal stress σ would facilitate the phosphorylation and creates a non-equilibrium steady state with increasing levels of cell contractility ρ and ATP

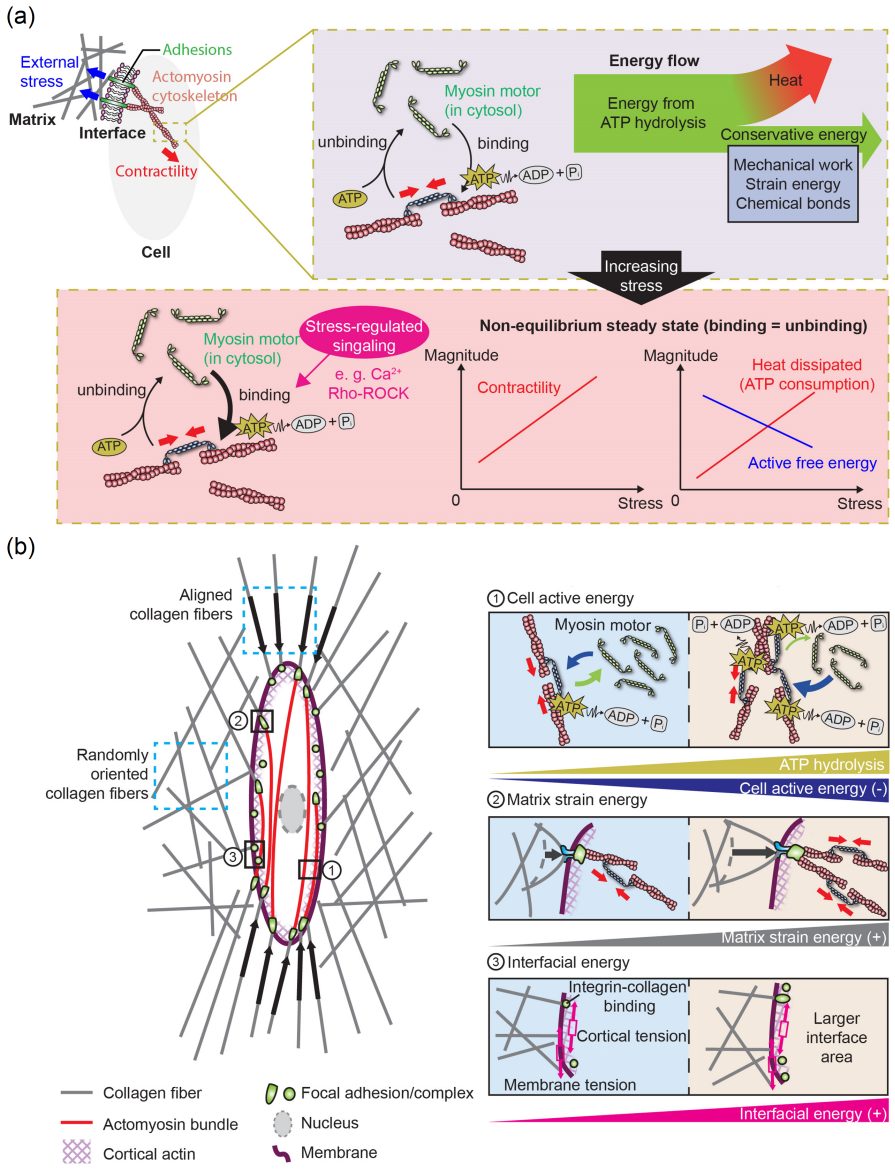

Figure 1: **Chemo-mechanical representation of the coupling between stress-regulated signaling and myosin motor recruitment regulated by ECM strain stiffening.** (a) When myosin motors undergo the cycle of binding, force generation and unbinding, cell contractility is maintained at a level proportional to the density of bound myosin. With ATP consumption required at each cycle, the energy released from ATP hydrolysis is converted into mechanical work and strain energy stored in the ECM as myosin motors contract the cytoskeleton until the steady state is reached, when the entire energy from ATP consumption is converted to heat. Stresses transmitted from the matrix through adhesions activate mechanosensitive signaling pathways, which upregulate the binding of myosin motors, leading to a steady state in which contractile forces and ATP consumption (dissipated as heat) vary with ECM stiffness. (b) schematization of the total free energy comprising the cell active energy, matrix strain energy and interfacial energy. Upon cell elongation and myosin motor recruitment, stresses polarize along the cell long axis, forming aligned contractile actin filaments. Such configuration correlates with an increased rate of ATP consumption characterized by a lower free energy. When the matrix is sufficiently stiff, contraction-induced deformation entails larger matrix strain energy. Finally, cell surface area is increased by its elongation, thereby increasing interfacial energy constituted from the integrin-collagen binding affinity, membrane and cortical tension. The competition among the above three energy components determines the optimal cell shape at steady state.

consumption. Accordingly, the active energy contributed by ATP hydrolysis must be added to the cell's conservative free energy. That is

$$\mathcal{U}_{\text{cell}} = \mathcal{U} - \int_{\xi=0}^{\rho} \kappa\left(\sigma\right) \Delta G \mathrm{d}\xi \tag{5}$$

where $\mathcal{U}$ represents the cell conservative energy constituted by mechanical, chemical and motility source terms (details are provided in Section 5.2), and the last term quantifies energy dissipation through ATP consumption. Next, due to the stress-dependent ATP hydrolysis being an exothermal process lowering the total free energy, the optimal cell shape is predicted by maximization of ATP consumption, hence minimizing the total free energy. The sequel expounds the general form of the total free energy constituted by the cell, cell-ECM interface, and that of ECM.

2.2 Generalized Steady-State Condition

The generalized steady-state condition can be attained through a two-step minimization process. First, the time rates of contractile strains and forces (alias *contractility*) must vanish within the cell. To this end, the complete time derivative of total free energy can be expanded in terms of principal strain and contractility components as [33]

$$\frac{\mathrm{D}\mathcal{U}_{\text{cell}}}{\mathrm{D}t} = \frac{\partial \mathcal{U}_{\text{cell}}}{\partial \rho_i}\frac{\partial \rho_i}{\partial t} + \frac{\partial \mathcal{U}_{\text{cell}}}{\partial \epsilon_i}\frac{\partial \epsilon_i}{\partial t} \tag{6}$$

which, after letting $\partial \rho_i/\partial t = \partial \epsilon_i/\partial t = 0$ at steady state, entails that the following be satisfied

$$\frac{\partial \mathcal{U}_{\text{cell}}}{\partial \rho_i} = \frac{\partial \mathcal{U}_{\text{cell}}}{\partial \epsilon_i} = 0 \tag{7}$$

Following the mathematical details presented in SI Appendix, Section 1.2, the following nonlinear equation system will be derived in terms of the principal stresses σ_i and strains ϵ_i:

$$\begin{cases} \sigma_i - \frac{\kappa(\sigma_i)}{\beta'} = \rho_0 + 3K'\epsilon_{\text{m}} + 2\mu'\widetilde{\epsilon}_i \\ \\ \rho_i - \frac{\kappa(\sigma_i)}{\beta'} = \rho_0 - \left(3K'_\rho\epsilon_{\text{m}} + 2\mu'_\rho\widetilde{\epsilon}_i\right) \end{cases} \tag{8}$$

where $3K' = 3K - 1/\beta$, $2\mu' = 2\mu - 1/\beta$ and $3K'_\rho = 2\mu'_\rho = 1/\beta$ define the effective bulk and shear moduli and their counterparts for motor density, respectively. Moreover, $\beta' = \beta/\Delta G$, and κ was defined in (4) as function of principal stresses.

Having obtained their principal components, the corresponding tensorial representation of stress and contractility can be determined from the polar decomposition theory as

$$\begin{cases} \boldsymbol{\sigma} = \sigma_i \boldsymbol{n}^{(i)} \otimes \boldsymbol{n}^{(i)} \\ \boldsymbol{\rho} = \rho_i \boldsymbol{n}^{(i)} \otimes \boldsymbol{n}^{(i)} \end{cases} \tag{9}$$

where summation is implied over i.

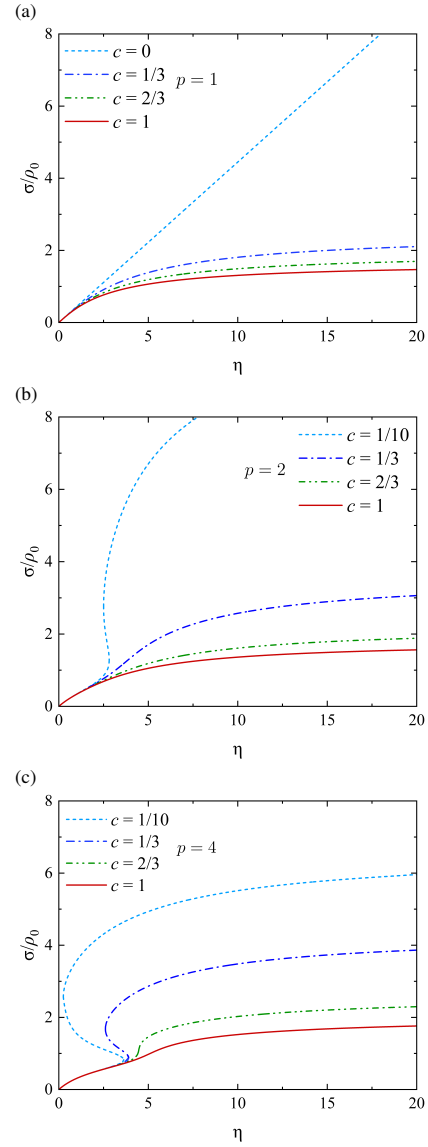

Figure 2: **Trizonal solution at varying tuning parameters** (p, c)**.** One-dimensional trizonal solution for normalized stress vs. equivalent stiffness ratio $\eta \equiv E_{\text{p}}/E$ at various tuning parameters of p ranging from 1 to 4 and c adopting (nearly) zero to 1. Cell parameters are identified by $E = 1.5$ kPa, $\nu = 0.27$, $(\varsigma, \mathcal{B}, \Lambda) = (0.2, 4.5, 1)$.

Provided the model parameters lie within their allowable ranges, Eq. (8) yields two possible solutions: one with limited contractility and corresponding polarization stress, and another with high contractility and corresponding polarization stress. Section 5.4 presents a mathematical expose' on the allowable ranges of the model parameters.

In the interest of better insight into model predictions

as well as its parametric range, we first simplify the cell-ECM domain into a one-dimensional subspace, where the cell is ideally connected to a micropost (with its stiffness denoted with K_{p}) or the cell is assumed to have a frozen spherical shape while being connected to a matrix with infinite radius. In order for better consistency with the general case, the post stiffness is conceived in terms of an equivalent matrix bulk modulus, whose equivalent Young's modulus is identified in proportion to that of the cell as $E_{\mathrm{M}} = \eta E$, hence letting $K_{\mathrm{p}} = E_{\mathrm{M}}/3(1-2\mu_{\mathrm{M}})$.

Figure 2 shows example plots of trizonal solution for stress and contractility vs. stiffness ratio η at varying modeling tuning parameters p and c for the special case of a cell connected to microposts. Note that the linear model is retrievable by letting $(p, c) = (1, 0)$. Increasing exponent p would chiefly decrease the upper-branch motility and contractile force level while increasing the unbinding-to-binding rate ratio c would would shrink the stiffness overlapping regime conducive to two possible cell shapes. Hence, equal binding and unbinding rates ($c = 1$) yields a neutral state with no or little distinction between lower and upper-branch motility levels and cell shapes. Altogether, tuning parameters best commensurate with physics of cell shape transition should lie within the ranges of $4 \leqslant p \leqslant 10$ and $0.3 \leqslant c < 0.6$.

3 Results

3.1 Optimum cell body aspect ratio at steady state

Recent time-lapse force microscopy outcomes has revealed that cells migrating in 3D matrices can maintain a constant shape between 30 to 60 minutes [59], which is sufficiently long compared to equilibrated contractility time scale (in the order of 10 minutes [60]). Hence, our energetics-based prediction at non-equilibrium steady state is applicable to cell shape transition during both single and collected migration.

Elongation of a cell under the effect of cell-ECM mechanosensitive signalling pathways (*e.g.* Ca^2+, Rho-ROCK) imparts significant alteration in the energetics of the entire domain. First, concentration of stresses near the elongated pole elevates stress upregulation of polarized signaling pathways thereby further recruiting myosin motors and formation of aligned contracted actin filaments, as indicated by increased first principal stress (σ_1) and contractility (ρ_1). Existing experimental results also demonstrate significantly higher actomyosin recruitment along with stronger bridging of focal adhesions by stress fibers in elongated fibroblasts on sufficiently stiff substrates [33, 35–37, 61]. Such increased actomyosin activity can be maintained by higher ATP consumption in the cell, reflected in reduction of the cell active energy $\mathcal{U}_{\mathrm{cell}}$ upon cell elongation. In regards to the matrix, the significant deformation conveyed to the matrix at the cell poles would increase the strain energy stored in the matrix $\mathcal{U}_{\mathrm{M}}$. Such increase would reflect as an energetic penalty that prevents cells from taking on infinite aspect ratios by reducing the level of energy consumption in the combined cell-ECM domain. To reflect this effect, the cell free energy and ECM strain and fibrous energies are superposed. Finally, the interfacial energy $\mathcal{U}_{\mathrm{int}}$ is majorly reflected in membrane-cortical and integrin binding, and minorly attributed to membrane strain energy (see Eq. (15)). Both components would increase with cell elongation, the former being in direct proportion to the cell outer surface area that increases with the cell body aspect ratio, and the latter due to elevated contractility stretching the adhesive bonds between the cell and ECM.

Altogether, the competition between decreasing cell-ECM and increasing interfacial energy components (Fig. 3a) leads to a non-monotonic profile of the total free energy $\mathcal{U}_{\mathrm{tot}}$ with respect to the cell body aspect ratio ζ (Fig. 3b). Therefore, evaluation of the optimum cell body aspect ratio at a given steady state solidifies into a secondary (post-processed) stage that follows the evaluation of total free energy in terms of the cell body aspect ratio and spotting the aspect ratio that corresponds to the minimum energy. Considering the larger decreasing and increasing slopes of energy curves when appearing in terms of their difference with those pertaining to a spherical cell ($\zeta = 1$), calculations were carried out in terms of $\Delta\mathcal{U} \equiv \mathcal{U} - \mathcal{U}(\zeta = 1)$. Note that COMSOL 5.6 was used to model and discretize the cell-ECM domain.

One can further observe variations in the energy profile under the effect of matrix stiffening in Fig's 3(c,d). The increasing effect of stiffness on the ECM strain energy would transpire as maintained optimum aspect ratio of 1 in the lower branch and reducing optimum aspect ratio towards 1 in the upper branch. Note that, due to its limited ATP consumption and contractility, the lower branch of the constitutive model can only predict (nearly) spherical cell shapes. Hence, $\mathcal{U}_{\mathrm{tot}}$ corresponding to the lower branch is normally a monotonically increasing function of cell body aspect ratio, thus its optimum realized at $\zeta = 1$. While the lower branch admits increasing level of total energy and ATP consumption with increasing ECM and cell body aspect ratio, the upper branch admits craters within the energy contours representing optimal cell body aspect ratio decreasing with stiffness.

The predicted optimum aspect ratios are next collected in plots against the ECM normalized stiffness η in Fig. 4. The normalized polarization parameter $\Lambda \equiv \alpha/\beta$, which quantifies the intensity of stress-regulated signaling pathways, would render the optimum steady-state cell body aspect ratio more sensitive to ECM stiffening. Moreover, it would reduce heterogeneity in cell motility by

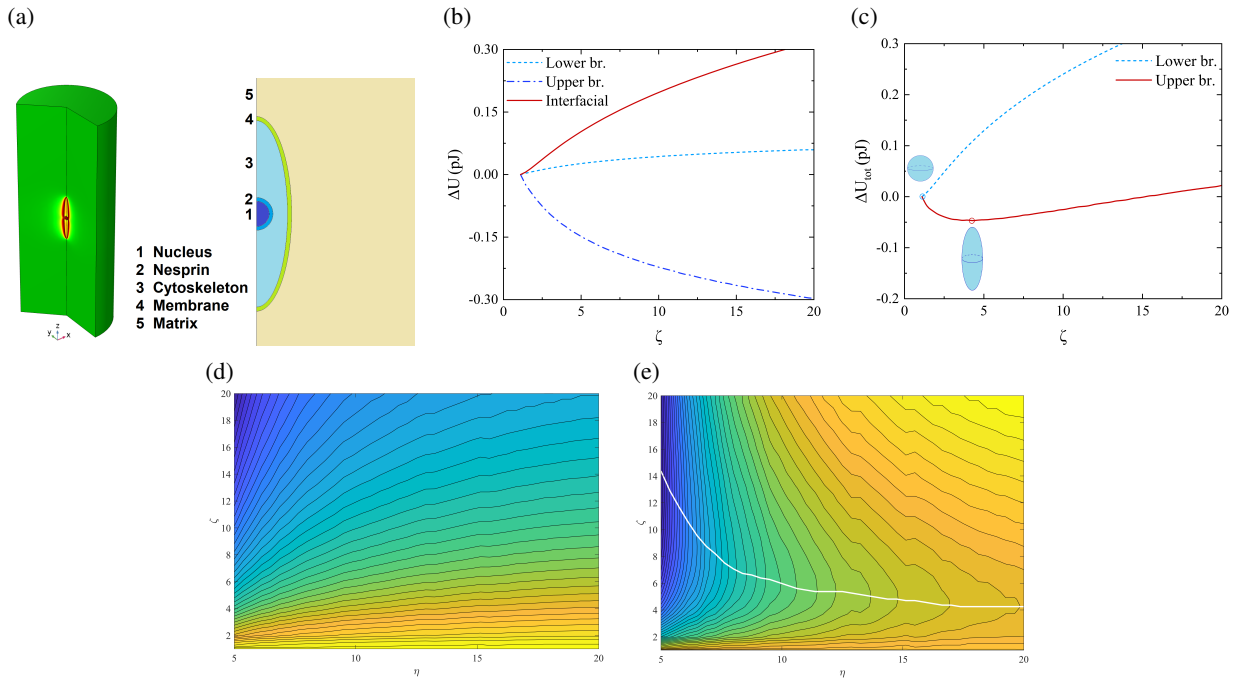

Figure 3: **Free energy-based stiffness-regulated optimal cell shape at equilibrium state.** (a) Constituents of the 3D computational model; (b) variation of cell–ECM free energy components (expressed as difference with those corresponding to the spherical cell) predicted by the lower and upper branches of stable solution to equilibrium equations, in comparison to the interfacial free energy counterpart, all vs. cell body aspect ratio ζ at a sufficiently high ECM to cell stiffness ratio $\eta \equiv E_{\mathrm{M}}/E = 5$; (c) total free energy differences from superposition of cell–ECM and interfacial contributions; (d,e) lower and upper branch iso-energy contours portraying cell body aspect ratio vs. ECM to cell stiffness ratio. Contour line canyons (connected into the superposed white line) denote optimum cell body aspect ratios. Cell parameters are identified by $E = 1.5$ kPa, $\nu = 0.27$, $(\varsigma, \mathcal{B}, \Lambda) = (0.2, 5, 0.7)$. Interfacial contribution is also identified by the parameter set $(\gamma_0, \gamma_1) = (0.2, 0.001)$ mN/m, $\delta_{\mathrm{ad}} = 1$. Model tuning parameters are also fixed at $(p, c) = (6, 1/3)$.

shrinking the overlapping range of η admitting heterogeneous shape distribution. Namely, larger stress polarization would clearly lower the minimum critical ECM stiffness that triggers metastasis. Smaller than infimum polarization parameters, however, would represent signaling detachment between the cell and ECM (Fig. 4a), hence predicting non-invasive spherical cells regardless of ECM stiffness.

Moreover, the same variation at varying membrane-cortical tension and adhesion density can be seen in Fig's 4(d,e). Intuitively, increasing the former would further withstand cell elongation due to higher membrane stiffness. All the same, increasing the latter would impair the cell's ability of adherance to and interaction with the matrix, hence downregulating actomyosin recruitment and inhibiting ATP consumption [22, 26–29]. Figure 5 sheds further light on the effects of model parameters on the optimal cell shape. Notably, the decreasing trend within ζ_{opt} vs. η might appear as contradictory with studies suggestive of increasing cell elongation and invasiveness with increasing ECM stiffness [30–34]. While all such studies are enlightening within their own confines, they all work around the transition zone, *i.e.* from below $\eta_{\mathrm{c}}^{(1)}$ up to slightly above this critical limit. Rather, only studies unfolding the biphasic correlation between cell invasiveness and ECM stiffness have posed the full-range correlation, yet failed to predict it analytically [38–40]. The apparent controversy between the two observed trends cannot be duly reconciled unless by taking into account the effect of heterogeneity in actomyosin recruitment at fixed motor density. Such heterogeneity has been unveiled in some relevant studies, yet without any effort for its analytical prediction [4–7].

Since the lower-branch solution prevalently delivers a spherical cell, the effect of model parameters can be explored for a sufficiently stiff matrix taken into account, *e.g.* for $\eta = 5$. Figure 5 presents the upper-branch steady-state optimum cell body aspect ratio ζ_{opt} in terms of nor-

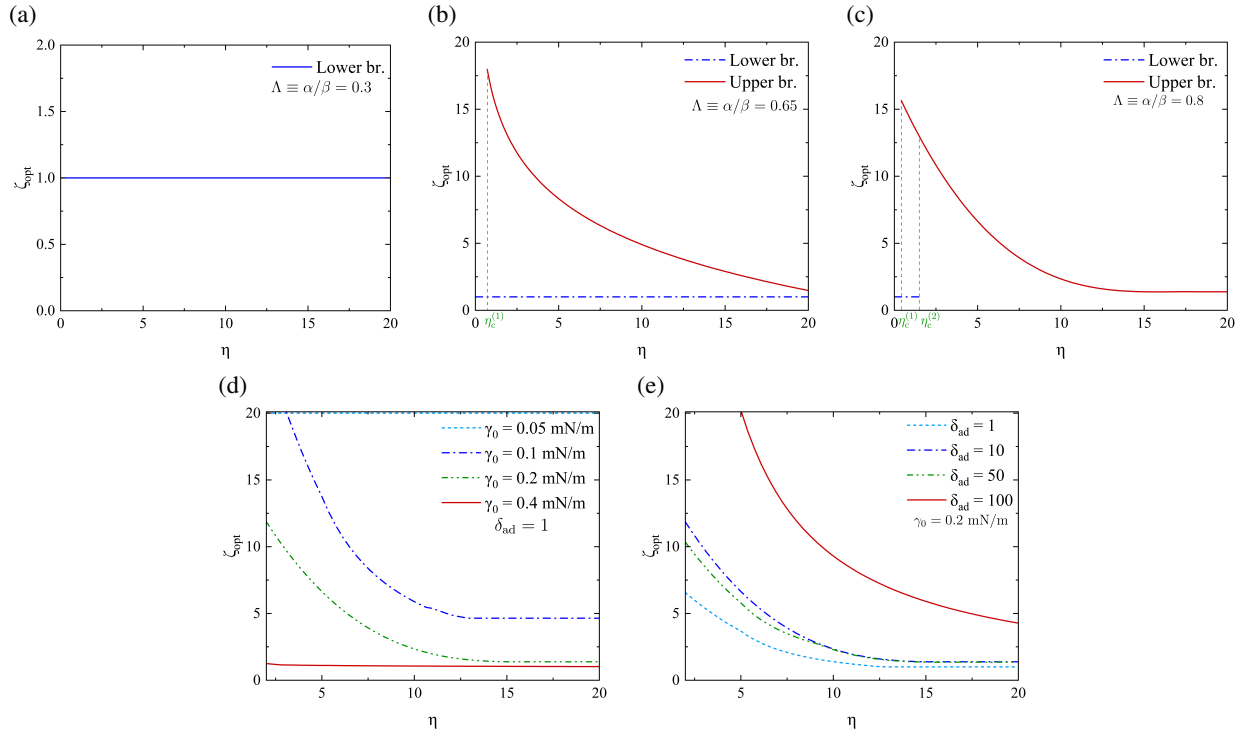

Figure 4: **Optimum cell body aspect ratio vs. ECM stiffness.** Variation of lower vs. upper-branch optimum cell body aspect ratio as function of the ECM to cell stiffness ratio $\eta \equiv E_{\mathrm{M}}/E$: (a–c) complete solution at various normalized polarization parameters $\Lambda \equiv \alpha/\beta$; (d,e) upper-branch (highly motile) solution at varying membrane–cortical tensile stiffness γ_0 (with $\delta_{\mathrm{ad}} = 1$) and integrin contribution δ_{ad} (with $\gamma_0 = 0.2$ mN/m), respectively. Other cell parameters are identified by $E = 1.5$ kPa, $\nu = 0.27$ and $(\varsigma, \mathcal{B}) = (0.2, 4.5)$. Adhesion binding affinity stiffness is also fixed at $\gamma_1 = 0.001$ mN/m. Model tuning parameters are also fixed at $(p, c) = (6, 1/3)$.

malized model parameters quantifying stress polarization ($\Lambda \equiv \alpha/\beta$), contractile density ($\varsigma \equiv \rho_0/E$) and chemo-mechanical coupling ($\mathcal{B} \equiv \beta E$) as well as interfacial parameters including membrane-cortical tensile stiffness γ_0 (mN/m) and normalized adhesion (integrin) density δ_{ad}.

As discussed beneath Fig's 4(a–c), polarization parameters below the infimum threshold represent signaling detachment between the cell and ECM while higher-than-infimum values are indicative of active ATP consumption. Nevertheless, larger values of Λ would trigger a steady state tending towards a stationary condition with small or zero myosin unbinding and net ATP consumption. This can be better perceived by referring to the primitive definition of α, which sets a nonlinear correlation between binding and unbinding myosin motor rates, *i.e.* $k_{\mathrm{on}} = (\alpha\sigma)^p\, k_{\mathrm{off}}$. As such, extreme enlargement of α would prohibitively enlarge the myosin binding rate so that ATP consumption and mechanosensitive signaling between the cell and ECM would be inhibited. Further, the antithetical influences of the interfacial energy terms can be envisaged in Fig's 5(c,d). It is witnessed that, below a certain limit, the tensile softening of the membrane would associate with significant increase in cell elongation and invasiveness. This condition represents membrane damage triggered by effects such as oxidative radiation [62], phenolic acids [63], or metal release processes [64]. All the same, the effect induced by integrin density is observed to escalate remarkably beyond a certain upper threshold that decreases considerably with membrane softening, *i.e.* lowering γ_0. Such abrupt increase in phenotype activity by increasing integrin contribution beyond this threshold is corroborated by earlier studies [22, 26–29]. The effects induced by contractile density ρ_0 and chemo-mechanical coupling β are likewise antithetical. Higher contractile densities would provide larger sources for ATP consumption and larger numbers of contractile dipoles per unit time, hence larger binding compared to unbinding rates, yielding more elongation and invasiveness of the cell [33]. Higher chemo-mechanical coupling, however, preserves chemo-mechanical energy transformation by inhibiting ATP consumption and non-conservative energy dissipation which, in turn, would pre-

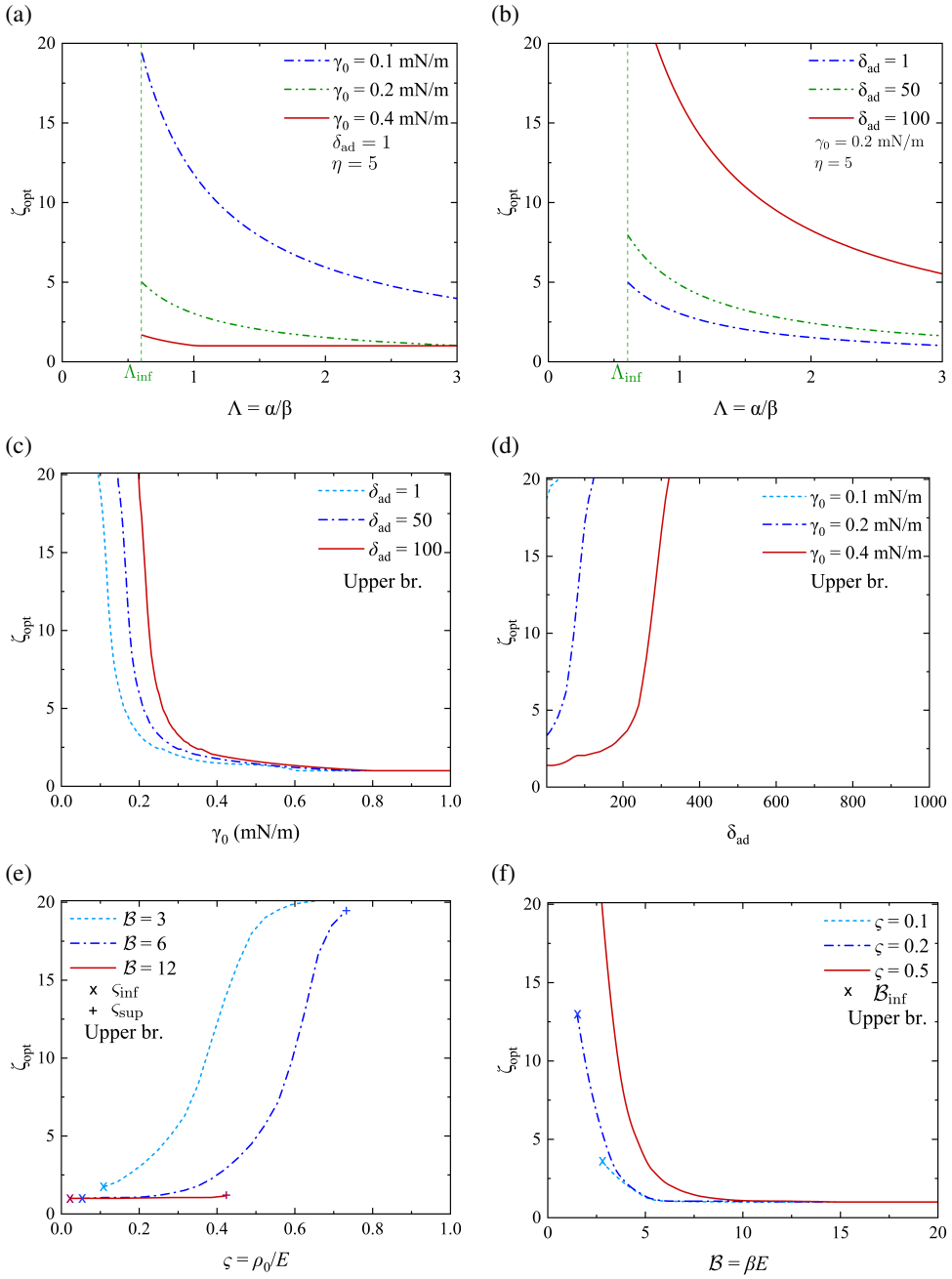

Figure 5: **Effect of model parameters on highly motile optimal cell shape.** (a,b) Upper-branch (highly motile) optimum cell body aspect ratio at a sufficiently high ECM to cell stiffness ratio of $\eta \equiv E_{\mathrm{M}}/E = 5$ in terms of normalized polarization parameter $\Lambda \equiv \alpha/\beta$, with $(\varsigma, \mathcal{B}) = (0.2, 4.5)$: (a) at varying membrane–cortical tensile stiffness γ_0 (with $\delta_{\mathrm{ad}} = 1$), (b) at varying integrin contribution δ_{ad} (with $\gamma_0 = 0.2$ mN/m); (c,d) in terms of γ_0 (with$\delta_{\mathrm{ad}} = 1$) and δ_{ad} (with $\gamma_0 = 0.2$ mN/m), respectively; (e,f) in terms of normalized contractility density $\varsigma \equiv \rho_0/E$ (at varying $\mathcal{B} \equiv \beta E$) and normalized chemo-mechanical coupling $\mathcal{B} \equiv \beta E$ (at varying $\varsigma \equiv \rho_0/E$), with $\Lambda = 0.75$. Other cell parameters are identified by $E = 1.5$ kPa, $\nu = 0.27$. Adhesion binding affinity stiffness is fixed at $\gamma_1 = 0.001$ mN/m. Model tuning parameters are also fixed at $(p, c) = (6, 1/3)$ (a–d) or $(p, c) = (8, 1/3)$ (e,f).

serve non-invasive cell shape [33].

3.2 Experimental Parametrization

Assessment of model parameteric predictability was gauged by adding the following reagents to the culture media of human HT1080 fibrosarcoma cells cultured in Dulbecco's modified Eagle medium, and subsequently embedded in low-density (1.66 mg/mL) and mid-density (3 mg/mL) bovine collagens [65] (see Section 5.1 for details): (*i*) Blebbistatin (20 μM, Sigma, 203391) and DMSO (0.1%, vehicle control, Sigma Aldrich) for actomyosin inhibition and its control culture, respectively; (*ii*) clone 4B4 mouse monoclonal anti-human CD29 (5 μg/mL, Beckman Coulter, 6603113) and mouse IgG1 isotype control culture (5 μg/mL, BD Bioscience, 557273); (*iii*) combination of Blebbistatin and clone 4B4 compared with the control culture with DMSO and IgG1 isotypes combined. Cell body aspect ratios (major over minor axis ratio) were approximated from mid-cellular cross sections exploiting an ellipsoid approximation plugin in Fiji/ImageJ (version 1.51).

As originally discussed in the Introduction, the terms *matrix stiffness* and *collagen density* are commonly used interchangably given the numerous references that have confirmed the direct correlation between the two [40, 65–70]. A popular method of evaluating matrix stiffness is through *Atomic Force Microscopy* (AFM), whereby a polystyrene microsphere is glued to a collagen cantilever and the resulting assembly, having fully dried, is subject to repeated contact force [66–69]. The force-displacement response is finally fitted into a Hertzian contact model which delivers the stiffness as a square-root function of contact displacement [71]. Accordingly, the low and intermediate bovine collagen densities would correspond to stiffness ratios approximated as $\eta = 1.75$ and $\eta = 3.5$, respectively.

The in-vitro histograms shown in Fig. 6 are the outcomes of a hybrid machine learning algorithm. The algorithm is constructed from two subroutines: one for parametrization and one for multimodal distribution. The former invokes a full-spectrum data library calculated from model predictions with varying contractile density according to the following variation law:

$$\bar{\rho_0} = \rho_0(1 + g_0\phi) \tag{10}$$

with g_0 denoting a coefficient obeying $0 < g_0 < 1$ (fixed at every case and varying from case to case) and $-1 \leqslant \phi \leqslant 1$. While g_0 sets the variation range of contractile density, its core value ρ_0 also varies such that $0.1 \leqslant \varsigma \equiv \rho_0/E \leqslant 0.6$. Besides varying g_0 and ς, the parametric library takes into account varying membrane–cortical tensile stiffness γ_0, integrin contribution $\delta_{\rm ad}$, and normalized stress polarization parameter Λ. Example plots with above variations vs. ϕ is shown in SI Appendix, Section 2.2.1.

Thereupon, the best parameter were firstly adopted such that the least squared difference is acquired between the model predictions and the main data peaks on the histogram of interest. Secondly, the percentage distribution was simulated by application of a replicated multimodal probability distribution subroutine. Note that bimodal distribution was found to generate the best coincidence with experimental histograms unless for the few cases with a large peak and monotonic distribution apart from it (where unimodal distribution was found optimal). No trimodal or higher-order distribution was found optimal at least within the range of data at hand. Note also that the nearly spherical cell body aspect ratios ($1 \leqslant \zeta < 1.2$) were predicted by the model's lower branch and higher ratios were evaluated using the upper branch.

The first effect explored pertains to matrix stiffening through varying collagen density (Fig. 6c). Having cultured isolated melanoma cell spheroids in bovine collagen, cells were separated from the melanoma and invaded the matrix [38]. At low collagen concentrations (*e.g.* 0.1 mg/mL), cells invading at the periphery of melanoma had a spherical dominant morphology. With first-level increase in collagen density (into 0.5 and 1.0 mg/mL), the cells became clearly elongated. Upon second-level increase, cells became more elongated with some common aspect ratios with the former plus other spindle-like cells protruding from melanoma.

The replicated histogram was achieved using the optimum parameter set identified by $g_0 = 0.75$, $\mathcal{B} = 5$, $\Lambda = 3$ (considered large enough to confine the entire range of $\zeta_{\rm opt}$ within the $[1, 5]$ range), $\varsigma = 0.2$ and interfacial parameters $\gamma_0 = 0.1$ mN/m, $\delta_{\rm ad} = 1$. Note that, since cells embedded in collagen densities clearly below 1.6 mg/mL were found to be insensitive to matrix stiffening, the model was tuned so as to predict $\eta = 1.75$ slightly above the minimum critical limit ($\eta_{\rm c}^{(1)}$) and $\eta = 3.5$ slightly above the maximum critical limit ($\eta_{\rm c}^{(2)}$), using tuning parameters of $(p, c) = (10, 0.5)$. Accordingly, increasing collagen density from 1.6 to 3 mg/mL would maintain a considerable overlapping range of aspect ratios (represented by the common area between histograms) and simultaneously transfer an additional percentage to the highly motile (upper) branch (the pink area protruded around $\zeta = 2$).

Next, actomyosin inhibition was investigated through treatment of HT1080 cells with Blebbistatin (Fig. 6d). While various local effects (including individual cell properties and local collagen fiber microstructures) can alter the measurable cell body aspect ratios, an overall decreasing effect is observable on cell elongation under such treatment, in comparison to the control culture treated with DMSO. It is thus conspicuous from the numeri-

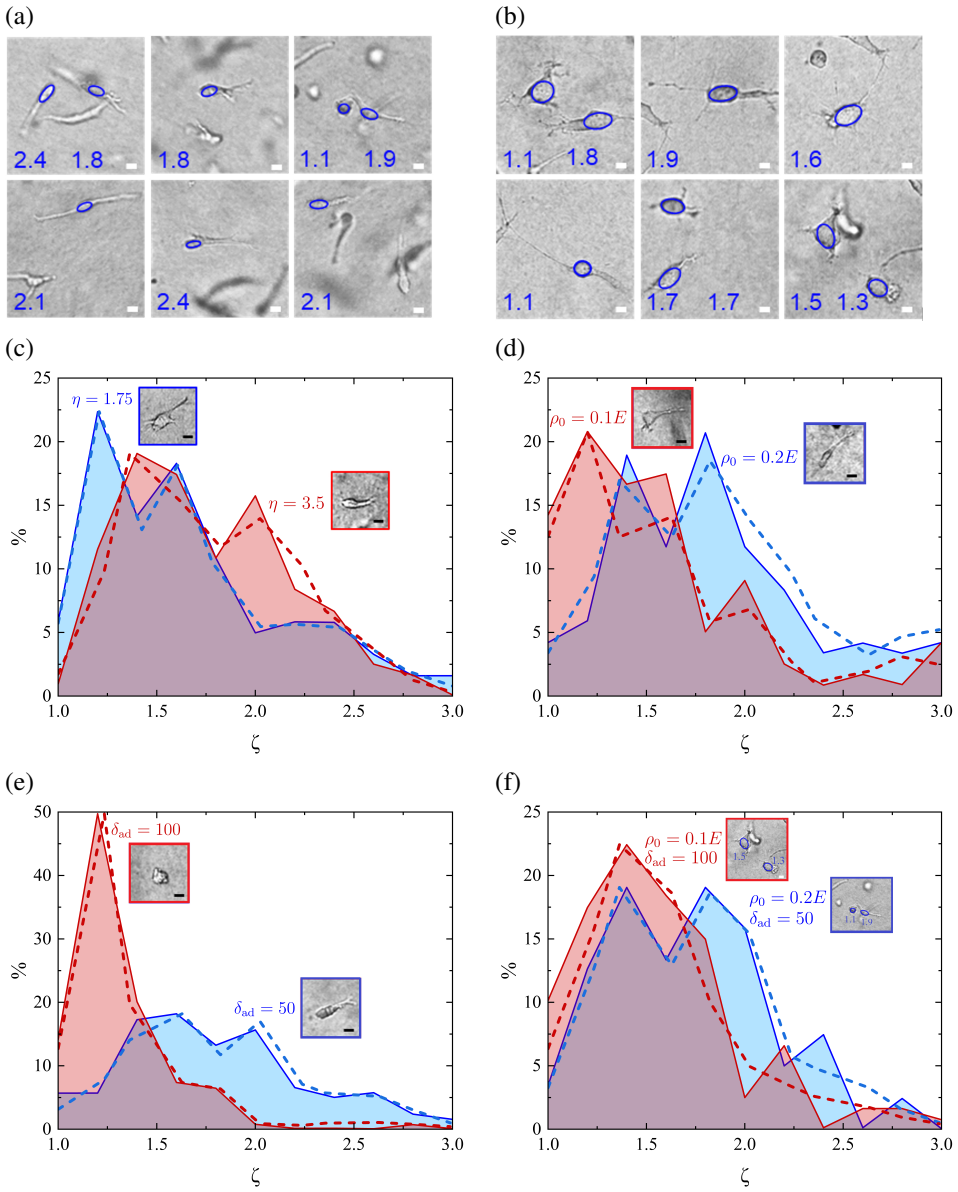

Figure 6: **Representative cell morphologies showcasing phenotype heterogeneity.** Morphogenesis of HT1080 cells migrating for 20 hours in 3 mg/ml bovine collagen with and without dual interference of myosin II-mediated cell contractility (Blebbistatin treatment) and β_1 integrin-mediated cell–ECM adhesion (4B4 treatment) recorded by bright-field microscopy: (a) example control assay treated with DMSO (0.1%, vehicle control, Sigma Aldrich) and mouse IgG1 isotype (5 μg/mL, BD Bioscience, 557273) controls; (b) example assay treated with Blebbistatin (20 μM, Sigma, 203391) and mouse monoclonal anti-human CD29 (clone 4B4, 5 μg/mL, Beckman Coulter, 6603113). Ellipses indicate cell bodies; values represent respective cell body aspect ratios. Scale bars are 10 μm. (c–f) Machine learning-based replicated in-vitro histograms of cell body aspect ratios cultured in variegated collagen matrices: (c) cells cultured in 1.6 and 3.0 mg/mL collagens, (d) cells treated with Blebbistatin compared with the DMSO control histogram, (e) cells treated with 4B4 mAb compared with the IgG1 isotype control histogram, (f) cells treated with combined Blebbistatin–4B4 mAb, compared with the DMSO–IgG1 control histogram.

cal histograms that decreasing the contractile density ρ_0 by the appropriate range is directly conducive to this effect. Note that an indirect path to numerical replication of such effect is through increasing the polarization parameter or its normalized equivalent Λ while being maintained above its lower bound Λ_{inf}. The reason lies intuitively in the direct correlation between the contractile density and mechanosensitive feedback triggered by stress polarization at a given cell steady state. Such effect is well commensurate with previous findings illustrating the effect of Y-27632 as a Rho-ROCK inhibitor [54]. Reduction of cell elongation thereunder further corroborates the essence of increased actomyosin activity for cell elongation and polarization.

Moreover, the 4B4 monoclonal antibody (mAb) treatment would impair collagen binding through $\beta 1$ integrins [72–74]. Through corresponding reduction of adhesion density δ_{ad} (Fig. 6e), cell elongation and polarization would be mitigated due to impairment of cell-matrix interaction, which downregulates mechanosensitive feedback, actomyosin activity and ATP consumption. Such effect is further commensurate with previous findings, *e.g.* reported by Castelló-Cros *et al.* who observed the same reduction effect on MDA-MB-231 cells under mAb13 treatment [74]. Note also that the effect of integrin impairment would render the aspect ration distribution unimodal, with its median driven towards unity, here around 1.2.

Ultimately, the biparametric calibration, invoking both optimum parameters used in Fig's 6(d,e), can well mimic the combined effect of treatment with Blebbistatin and 4B4 antibody compared with control treatment with DMSO and IgG1 isotype. To be importantly noted, just as mere variation of collagen density (Fig. 6c) would prompt higher dispersity of the aspect ratio for its values up to 2, so too would both simultaneous treatments (Blebbistatin–4B4 and DMSO–IgG1). Existence of large diversity within cell shapes inside this range warrants the demand for a trizonal model that can easily output the largely distinct cell shapes at every given percentage. To be secondarily noted, upon treatment of HT1080 cells with Blebbistatin, as well as its combined (DMSO–IgG1 or Blebbistatin–4B4) treatment, cells can turn quite dendritic with long protrusions oriented from several positions on the cell surface. Hence, obtaining an accurate estimate of the aspect ratio would entail fitting an ellipse to the innermost cell boundary (as proposed by Thievessen *et al.* [75]).

4 Discussion

Via the homographic representation of ATP consumption rate in Eq. (4), it was shown that, through stress-regulated formation of actin bundles and recruitment of myosin motors, two ranks of metabolic activity would be achieved. Thereupon, the lowly motile rank is associated with limited intracellular contractility, non-invasive (round) cell shape and independence upon extracellular stiffness. All the same, the highly motile rank would deliver high intracellular contractility, invasive (elongated) cell shape and pronounced dependence upon extracellular stiffness. Last, the overlapping zone between the two ranks would envelope a finite range of cell states with both possible levels of contractility and elongation that is well correlated with present and previously reported experiments [4–7]. The lower bound to the overlapping zone would then determine a minimum level of ECM stiffness (or an equivalent minimum collagen density) that triggers maximal cell invasiveness. Up to this level of stiffness, cell migration is intrinsic to sufficiently stiff environments (thus its name *durotaxis*) as a consequence of energy minimization. On the other hand, the upper bound to the overlapping zone would determine the maximum ECM stiffness level that characterizes cell invasion, beyond which the cross-linkage among ECM fibers would substantially reduce cell elongation and invasiveness [38–40]. While some recent models tend to account for the anisotropic nature of stress-regulated signaling pathways [16, 49, 50], such models fail to capture the salient physical features of cell contractility and elongation in terms of ECM stiffening due to the abrupt (first-order) shape transition characteristic of such models as well as failure to predict heterogeneity in motility levels.

Since steady-state cell shape is directly relevant to the competition amongst cell free energy, cell-ECM interfacial energy and ECM strain energy, the impact of pharmacological treatments on cell configuration best reflects in the energetics of both the cell and ECM. The myosin inhibiting trace of Blebbistatin in Section 3.2, for instance, has been likewise observed from similar treatment on human bronchial epithelial cells (HBECs) [61]. Therein, Blebbistatin treatment would downregulate both actomyosin contractility and glycolysis through inhibiting myosin II accompanied by isolation of actin monomers and shrinkage of F-actin bundle lengths. The observed feedback among substrate stiffness, actomyosin activity and glycolytic rate lends further credibility to the introduced durotaxis model. Meanwhile, fibroblasts treated with Blebbistatin would turn considerably more dendritic and generate long, densely populated protrusions. While the observed fibroblast shapes did not reveal strong correlation with treatment dosage, future studies can investigate the possible correlation between cell elongation and protrusion growth. As schematically shown in Fig. 7b, collagen fibers realign in the direction of stress-regulated polarization, providing contact guidance for formation of protrusions. Accordingly, an elongated cell tends to develop protrusions at both poles.

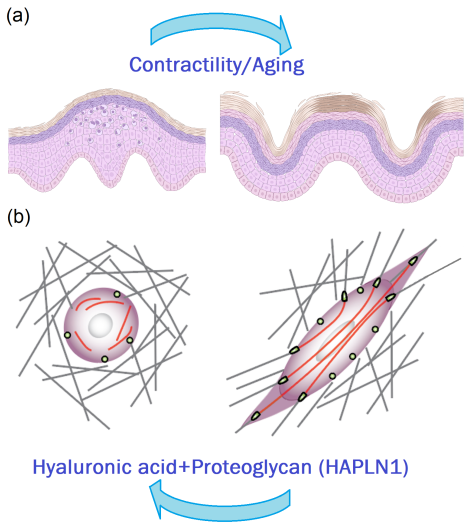

Figure 7: **Extracellular strain stiffening and stiffness degradation can both instigate malignant phenotypes.** (a) Schematic histological sections of young vs. aged human skin, whereby young skin admits an overly stiff basket-weave pattern whereas aging is characterized with extracellular stiffness degradation and alignment of senescent fibroblasts [42, 43]; (b) corresponding schematic cell morphology in young vs. aged skin, with elongation and ECM fiber-mediated protrusion prompted by interactive intracellular actomyosin contractility and extracellular stiffening as well as fiber alignment. Hyaluronic acid and Proteoglycan (HAPLN1) is a conducive method for reversal of the aging process [39].

A similar effect to that imparted by Blebbistatin treatment is achievable from hyaluronic and proteoglycan link protein (HAPLN1) in aged skin fibroblasts to revert realignment of fibroblasts in stiff matrices (Fig. 7) [39, 41–43]. In a recent endeavour by Kaur *et al.*, such reconstruction was analyzed using the established in-vitro *cell-derived matrix* (CDM) technique to fabricate ECM and recapitulate aging-induced fiber realignment by mere means of fibroblasts [39]. They further extended the in-vitro date into an in-vivo model by through assessment of ECM structure in young vs. aged C57BL/6 mouse skins. In both models, remarkable difference was observable between young and aged fibroblasts in the sense that malignant cell migration would be promoted in dermal substrates whose stiffness had been degraded by age-related fibroblast realignment. Application of HAPLN1 would then reverse the dermal degradation mechanism whereby the so-called *basket weave* structure would be retrievable. The trizonal predicted cell elongation vs. ECM stiffness is true to the spirit of demoted cell contractility and elongation on overly stiff and HAPLN1-restructured substrates. This adds another layer of credibility to the proposed model. In more general sense, the demoted actomyosin activity and cell elongation inside overly stiff matrices is best reflected in the effect of reduced pore size with increasing collagen concentration. Thereupon, the confinement from collagen densification would preclude fibers from realignment, hence limiting cell shape transition. In particular, in an environment where matrix pores are much smaller compared to the cell volumes, cells must degrade and remodel the ECM network by secreting matrix metalloproteinase (MMP) before shape transition can occur. Therefore, in a non-degradable matrix or with deficient MMP secretion, cells would adapt to the shape of network pores [65, 76].

Insofar as the effect of cell-ECM adhesion is concerned, the effect induced by 4B4 antibody is similar to that mediated by *vinculin knockout* fibroblasts, which inhibit contractile force transmission from the cell on the surrounding matrix. Consequently, the cells would exhibit limited elongation and polarization [75]. By the same token allowing for predicting the effect of the 4B4 integrin inhibitor, the present model can very well quantify the sequestering effect of vinculin knockout fibroblasts. In fact, the formerly defined adhesion density δ_{ad} represents the density of collagen ligands connected to the cytoskeleton. Hence, cells would adopt less elongated configuration with fewer available ligands. Thus far, we have deemed no interdependence between interfacial parameters and the cell shape, hence rendering optimal cell shape function in terms of independently arbitrated membrane-cortical stiffness γ_0 and adhesion density δ_{ad}. While such approach is both qualitatively and quantitatively true to the spirit of cell shape transition, relevant studies allude to possible correlation at least between adhesion binding (mainly through integrins) and the instantaneous (unsteady) cell configuration [22]. Another line of prospective research would thus examine such possible correlation.

5 Materials and Methods

5.1 Human cell culture and 3D collagen matrix

In order to assess the predictive capability of the proposed energy-based modeling framework, human HT1080 fibrosarcoma cells (ACC315; DSMZ Braunschweig) were cultured in Dulbecco's modified Eagle medium (DMEM; Sigma Aldrich), supplemented with 10% fetal bovine serum (FBS; Sigma Aldrich), penicillin (100 U/mL), streptomycin (100 mg/mL; PAA), and sodium pyruvate (1 mM; Thermo Fisher Scientific). Cell identity was verified by the Assay coded SNP–ID (from the Sequenom, MassArray System, Characterized Cell Line Core Facility, MD Anderson Cancer Center, Houston, TX), and freedom from contamination with mycoplasma was regu-

larly verified using the MycoAlert Mycoplasma Detection Kit (Lonza). Cells from the sub-confluent culture were subsequently detached by trypsin-EDTA (2 mM, Sigma Aldrich) and embedded in low-density (1.66 mg/mL) and mid-density (3 mg/mL) bovine collagens (PureCol, Advanced Biomatrix) [65]. Following collagen polymerization (at 37°C for 20–30 minutes), single-cell cultures in the 3D collagen were submerged in the culture medium and maintained at 37°C. Finally, cell shape of individual cells were measured in 3D collagen cultures after 24 hours after the setting of single-cell spreading.

All antibodies and inhibitors used were purchased as azide-free or dialyzed (Slide-A-Lyzer mini dialysis device, 20 MWCO) compounds. Single-cell cultures in 3D collagens were incubated (37°C for 20h), and cell shapes were monitored by 3D brightfield microscopy (20X/0.30 HI Plan objective, DM IL LED microscope, Leica). Z-stacks were recorded, with one in-focus slice of each cell used for analysis. Cell body aspect ratios (major over minor axis ratio) were approximated from mid-cellular cross sections exploiting an ellipsoid approximation plugin in Fiji/ImageJ (version 1.51).

5.2 Energetics of cell-ECM system

The two-way feedback between the cell and ECM reflects in superposition of three sources of free energy: cell, the cell-ECM interface, and ECM itself, hence reading $\mathcal{U}_{\rm tot} = \mathcal{U}_{\rm cell} + \mathcal{U}_{\rm int} + \mathcal{U}_{\rm M}$. First and foremost, the cell active free energy is superposed by an active, a passive and a nonconservative component from ATP consumption:

$$\mathcal{U}_{\rm cell} = \mathcal{U}_{\rm act} + \mathcal{U}_{\rm pas} - \int_{\xi_i=0}^{\rho_i} \kappa\left(\sigma_i\right) \Delta G \mathrm{d}\xi_i \tag{11}$$

where $\kappa(\sigma_i)$ was introduced in (4). The former reflects the energy involved in the myosin-mediated cell contraction of the cell, and the effect of stress polarization on actomyosin networks through mechanosensitive pathways (*e.g.* Ca^2+, Rho-ROCK). The tensorial image of the contractility of myosin motors ρ_{ij} is reflective of force dipoles with i and j indices denoting the force component and the direction along which the force is offset, respectively [35, 77, 78]. It is assumed, in the stress-free (quiescent) state, that contractility is uniform throughout the cell, with its magnitude denoted with ρ_0. Accordingly, the active energy consists of the chemical energy associated with myosin recruitment (ATP hydrolysis) and the mechanical work from conversion of ATP hydrolysis to motor work:

$$\mathcal{U}_{\rm act} = \mathcal{U}_{\rm chem} + \mathcal{U}_{\rm mot} \tag{12}$$

where

$$\mathcal{U}_{\rm chem} = \frac{\beta}{6}\left(\rho_{kk} - 3\rho_0\right)^2 + \frac{\beta}{2}\tilde{\rho}_{ij}\tilde{\rho}_{ij}$$
$$\mathcal{U}_{\rm mot} = \rho_{\rm m}\epsilon_{kk} + \tilde{\rho}_{ij}\tilde{\epsilon}_{ij}$$

with the $\tilde{(\cdot)}$ script denoting deviatoric components.

All the same, inasmuch as the cell is presumably composed of the nucleus (idealized with a central sphere), nesprin (idelized with an interfacial layer between the nucleus and cytoskeleton) and cytoskeleton (Fig. 8a), the passive energy component portrays the strain energy stored therein when deformed by contractile forces. That is

$$\mathcal{U}_{\rm pas} = \int_{\Omega_{\rm nuc}} W_{\rm nuc}\left(\epsilon_{ij}\right) \mathrm{d}\Omega + \int_{\Omega_{\rm nes}} W_{\rm nes}\left(\epsilon_{ij}\right) \mathrm{d}\Omega + \int_{\Omega_{\rm cyt}} W_{\rm cyt}\left(\epsilon_{ij}\right) \mathrm{d}\Omega \tag{13}$$

where W's denote the respective strain energy densities as functions of strain. In order for the above energy terms to correspond to a steady state, the last term should be expressed explicitly in terms of strain components so differentiation with respect to them turns out convenient. With the cytoskeletal deformation maintained within the elastic regime, the last term can be transformed into $\mathcal{U}_{\rm mech}$, expressible as strain energy minus the mechanical work done thereby. Each term can be resolved into two parts resulting from the mean and deviatoric strain components as

$$\mathcal{U}_{\rm mech} = \mathcal{U}_{\rm s} + \mathcal{W} \tag{14}$$

where

$$\mathcal{U}_{\rm s} = \frac{K}{2}\epsilon_{kk}^2 + \mu\tilde{\epsilon}_{ij}\tilde{\epsilon}_{ij}$$
$$\mathcal{W} = -\left(\int_0^{\epsilon_{kk}} \sigma_{\rm m}\mathrm{d}e_{kk} + \int_0^{\tilde{\epsilon}_{ij}} \tilde{\sigma}_{ij}\mathrm{d}\tilde{e}_{ij}\right)$$

with $0 \leqslant e_{ij} \leqslant \epsilon_{ij}$, hence $0 \leqslant e_{kk} \leqslant \epsilon_{kk}$ and $0 \leqslant \tilde{e}_{ij} \leqslant \tilde{\epsilon}_{ij}$ denoting integral variables.

Moreover, interfacial energy represents the contributions from adhesions (mainly integrins), actin cortex and the basement membrane. The interface is here idealized as a thin layer with uniform thickness that connects the cytoskeleton to the matrix (Fig. 1a). Adhesion receptors (mainly integrins) maintain spontaneous binding to complimentary collagen ligands, which results in reduced free energy [38]. Hence, the cell tends to adopt an elongated shape at higher receptor densities to maximize the number of bonds with the matrix. On the other hand, the membrane-cortical tension together tend to shrink the surface area, not favoring cell elongation. Altogether, the combined effect of membrane-cortical tension and adhesion receptors can be expressed in terms of a factor of cell body surface area as

$$U_{\rm int} = \left(\gamma_0 - \gamma_1\delta_{\rm ad}\right)\mathcal{S} \tag{15}$$

with γ_0 denoting the contribution of membrane-cortical tension, γ_1 reflecting the change of energy associated with the formation of each receptor-ligand bond, and $\delta_{\rm ad}$ being a scaling factor representing the density of adhesion receptors. Finally, $\mathcal{S}$ represents the cell outer surface area

which, for a prolate spheroidal cell, obeys

$$\mathcal{S} = 2\pi b^2 \left(1 + \frac{\zeta}{e} \arcsin e\right)$$

where $\zeta = a/b \geqslant 1$ is the cell body aspect ratio (with $\zeta \geqslant 1$ being characteristic of a prolate cell) and $e^2 = 1 - \frac{1}{\zeta^2}$ denotes the spheroid eccentricity.

Finally, matrix energy is constituted partially by the strain energy stored in ECM by the cell's contractile forces (through adhesion receptors) and partially by fibers. The latter is contributed by diffuse and aligned fibers. Diffuse fibers are randomly dispersed throughout the matrix and buckled along the principal compressive stresses while aligned fibers are stretched along the tensile principal stresses. Accordingly, the combined energy contributed by ECM fibers can be considered to admit a nearly incompressible Neo-Hookean constitutive model with a quadratic-type energy expression [45]. That is, the combined ECM strain energy density reads

$$W_{\mathrm{M}} = \frac{\mu_{\mathrm{M}}}{2}\left(\frac{\sum_{i=1}^{3}\lambda_i^2}{(\lambda_1\lambda_2\lambda_3)^{2/3}} - 3\right) + \frac{K_{\mathrm{M}}}{2}\left(\lambda_1\lambda_2\lambda_3 - 1\right)^2 + \sum_{i=1}^{3} f\left(\lambda_i\right) \tag{16}$$

where the last term is provided by aligned fibers and the previous terms represent randomly dispersed fibers. Here, μ_{M} and K_{M} denote the matrix shear and bulk moduli, and λ_i $(i = 1, 2, 3)$ are the three principal stretches. The power-law function f, hereby introduced to capture fiber-mediated matrix stiffening in the tensile principal directions, is a piecewise function obeying

$$f\left(\lambda_i\right) = \begin{cases} 0 \quad , \quad \lambda_i < \lambda_{\mathrm{L}} \\ E_{\mathrm{f}} \frac{(\lambda_i - \lambda_{\mathrm{L}})^{n+2}(\lambda_{\mathrm{U}} - \lambda_{\mathrm{L}})^{-n}}{(n+1)(n+2)}, \lambda_{\mathrm{L}} < \lambda_i < \lambda_{\mathrm{U}} \\ E_{\mathrm{f}}\left[\frac{\lambda_{\mathrm{U}}(\lambda_i - \frac{1}{2}\lambda_i^2)}{n+1} + \frac{(1-\lambda_{\mathrm{U}}+\lambda_i)^{m+2} - (m+2)\lambda_i}{(m+1)(m+2)}\right], \lambda_i > \lambda_{\mathrm{U}} \end{cases} \tag{17}$$

where E_{f} denotes fibers' Young's modulus, and

$$\left(\lambda_{\mathrm{L}}, \lambda_{\mathrm{U}}\right) = \lambda_{\mathrm{c}} \mp \frac{\lambda_{\mathrm{c}} - 1}{8}$$

where λ_{L} (using $-$) and λ_{U} (using $+$) are, respectively, the lower and upper bounds to the interpolation range, so formulated as to ensure a continuous derivative around the transition point identified by the critical stretch λ_{c}. Correspondingly, f is primarily aimed to distinguish between loose (randomly oriented) fibers (with vanishing principal stresses) from aligned fibers (with power-like hardening), with the transition in between determined by λ_{c}.

5.3 One-dimensional special case

Recollecting Eq. $(8)_1$, only one independent or nonzero stress-strain conjugate exists in the 1D special case. That is, assuming the nonzero stress-strain conjugate at the cell-post interface or the uniform stress-strain conjugate at the cell-ECM interface is denoted with σ and ϵ, the correlation obeys $\epsilon = -2\sigma/K_{\mathrm{p}}$ and $\epsilon \equiv \epsilon_{\mathrm{rr}}\left(R\right) = \epsilon_{\theta\theta}\left(R\right) = -\sigma/2\mu_{\mathrm{M}}$, respectively. For the latter case, the reader can consult the solution for a sphere with internal pressure [79]. Therefore, the general 1D model solidifies into the solution to the equation identified by $Y_1 = Y_2$, where

$$\begin{cases} Y_1 = \frac{\kappa\left(\frac{\sigma}{\rho_0}\right)}{\rho_0 \beta'} \\ Y_2 = -1 + \left(1 + \frac{\gamma\mathcal{G}}{\eta}\right)\frac{\sigma}{\rho_0} \end{cases} \tag{18}$$

where γ and $\mathcal{G} = g - 1/\mathcal{B}$ are problem-dependent dimensionless parameters, such that

$$\gamma = 2 \quad , \quad g = \frac{1-\nu}{(1+\nu)(1-2\nu)}$$

for the cell connected to microposts, and

$$\gamma = 1 + \nu \quad , \quad g = 1 - 2\nu$$

for the spherical cell connected to infinite ECM. Moreover, $\mathcal{B} = \beta E$ and the rest of parameters were defined in advance.

In the general sense, Eq. (18) delivers a spectral solution comprising one, two or three solution branches. Accordingly, the solution branch is governed by case-wise comparison between the line slope $(1/\eta)$ with the two slopes of tangency between Y_1 and Y_2, here denoted with critical slopes $\eta_{\mathrm{c}}^{(1)}$ and $\eta_{\mathrm{c}}^{(2)}$ as schematized in Fig. 8c. At the points of tangency, simultaneous satisfaction of $Y_1\left(\frac{\sigma}{\rho_0}\right) = Y_2\left(\frac{\sigma}{\rho_0}\right)$ and $Y'_1\left(\frac{\sigma}{\rho_0}\right) = Y'_2\left(\frac{\sigma}{\rho_0}\right)$, utilizing $\frac{\sigma}{\rho_0} = \frac{1}{\alpha\rho_0}\left(\frac{\kappa}{1-c\kappa}\right)^{1/p}$ which expresses σ in terms of κ, the following equation can be reached:

$$\begin{aligned} &\kappa_{\mathrm{c}}^2 - q'\kappa_{\mathrm{c}} + \rho\prime_0\beta'\left(1-q\right) = 0 \;\therefore\; \kappa_{\mathrm{c}} = \frac{1}{2}\left(q' \pm \sqrt{\Delta}\right) = \{\kappa_{\mathrm{c}}^{(1)}, \kappa_{\mathrm{c}}^{(2)}\} \\ &\eta_{\mathrm{c}} = \frac{\gamma\mathcal{G}}{-1 + \frac{p\alpha}{\beta'}\kappa_{\mathrm{c}}{}^q\left(1 - c\kappa_{\mathrm{c}}\right)^{2-q}} = \{\eta_{\mathrm{c}}^{(1)}, \eta_{\mathrm{c}}^{(2)}\} \end{aligned} \tag{19}$$

where $\Delta = q'^2 - \frac{4}{p}\rho\prime_0\beta'$ is the equation discriminant, with $q = 1 - 1/p$ and $\left(q', \rho'_0\right) = \frac{1}{c}\left(q, \rho_0\right)$.

Figure 8 shows a schematic representation of the 1D solution through varying intersection between Y_1 and Y_2, mathematical notion of the critical stiffness ratios corresponding to tangential contact between Y_1 and Y_2, and an example trizonal solution for stress and contractility vs. stiffness ratio η. The existence of two distinct motility levels, with the upper level exeeding twice the lower level with the adopted parameters, is conspicuous.

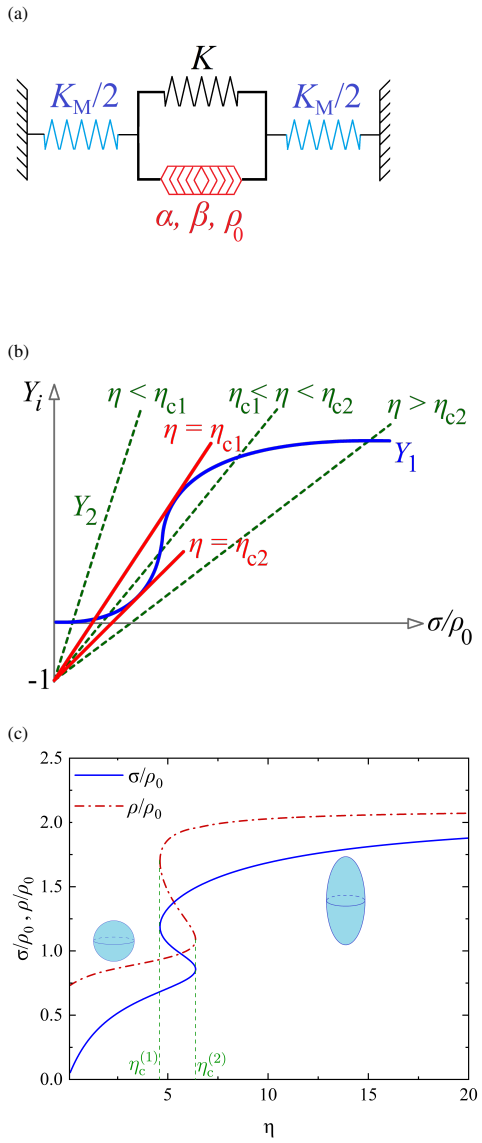

Figure 8: **Mathematical representation of the trizonal durotaxis model.** (a) 1D cell-ECM model consisting of linear elements (passive cell stiffness attached to ECM stiffness) and a nonlinear active element; (b) schematic 1D solution scheme from intersection between the stress-dependant nonlinear term and stiffness-dependant linear term, revealing two critical stiffness ratios $\eta_c^{(1)}$ and $\eta_c^{(2)}$ determining the bounds to solution branches; (c) example complete 1D solution (with $p = 8$) delivering stress and contractility over three branches, with cell and parameters identified by $E = 2$ kPa, $\nu = 0.3$, $(\varsigma \equiv \rho_0/E, \mathcal{B} \equiv \beta E, \Lambda \equiv \alpha/\beta) = (0.15, 6, 1)$, which delivers $\rho_0 = 0.3$ kPa $\beta = 3$ 1/kPa and $\alpha = \beta$.

Upon generalization of the model into 3D domains, the lower and upper branches are predominantly conducive to spherical (non-invasive) and elongated (metastatic) cells, respectively. Note that, albeit mathematically true, the middle declining portion in the overlapping (middle) branch is nonphysical considering the essential condition of stress and contractility elevation with the matrix being stiffened. Hence, the middle solution will be disregarded in the general (3D) model implementation.

5.4 Asymptotic analysis and allowable parameter ranges

Several mathematical constraints would restrict the ranges of allowable values for the model parameters. Before the steps are set forth, note that, as later confirmed in Section 3.1, the lower-branch solution would predominantly predict a spherical cell shape. Hence, the same parameter ranges derived herein for the special case of a spherical cell inside an infinite matrix can be later applied to general 3D cell-ECM domains with elongated (spheroidal) cell shapes.

By primitive definition, model tuning parameters p and c should adopt ranges that guarantee the trizonal solution. Accordingly, $0 < c \leqslant 1$ and $p > p_{\text{inf}}$, where the infimum power p_{inf} is determined by the nonnegativity condition of discriminant Δ. That is

$$\Delta > 0 \;\therefore\; p > p_{\text{inf}} = \left[1 + 2\mathcal{B}'\varsigma\left(1 - \sqrt{1 + \frac{1}{\mathcal{B}'\varsigma'}}\right)\right]^{-1} \tag{20}$$

where $\mathcal{B}' = \beta' E$ (with β' defined in advance) and $\varsigma' = \frac{1}{c}\varsigma$ with $\varsigma = \rho_0/E$. While (20) sets a lower limit to exponent p, it should be maintained well above the upper bound to this infimum at high levels of contractile density and/or chemo-mechanical coupling. The latter upper bound, as shown in Fig's 9(e,f), is mathematically set by the $\mathcal{B}'\varsigma$ approaching infinity. Naming this product $\chi = \mathcal{B}'\varsigma = \beta'\rho_0$, one can obtain the supremum to p_{inf} from its asymptotic value at $\chi \longrightarrow \infty$. To this end, the emerging $\infty - \infty$ ambiguity can be resolved by replacement of function $f(\chi) = \sqrt{1 + \frac{c}{\chi}}$ by its Taylor series, with $1/\chi$ transformed into a new variable such as t, thus $f(t) = \sqrt{1 + ct}$. Namely

$$\begin{aligned}\lim_{\chi\to\infty} f(\chi) \equiv \lim_{t\to 0} f(t) &= \lim_{t\to 0}\left(f(0) + f'(0)t\right) \\ &= \lim_{t\to 0}\left(1 + \frac{c}{2}t\right) = \lim_{\chi\to\infty}\left(1 + \frac{c}{2\chi}\right)\end{aligned} \tag{21}$$

which delivers the following asymptotic limit to p_{inf}:

$$\sup(p_{\text{inf}}) = \lim_{\chi\to\infty}\left[1 + 2\chi\left(1 - f(\chi)\right)\right]^{-1} = \frac{1}{1-c} \tag{22}$$

that entails adopting powers beyond this limit, *i.e.* $p > \frac{1}{1-c}$. For $c = 1/3$, for instance, the above supremum turns out 1.5 as shown in Fig's 9(e,f).

Next, we evaluate the allowable range for the stress polarization parameter α, in its normalized form $\Lambda = \alpha/\beta$. The general condition for this parameter is set by nonnegativity of η_c in Eq. (19), which requires

$$\Lambda' > \frac{1}{p{\kappa_c}^{1-1/p}\left(1-c\kappa_c\right)^{1+1/p}} \tag{23}$$

where $\Lambda' = \alpha/\beta'$. The lower limit to Λ', however, can be evaluated from the minimum discriminant, *i.e.* $\Delta = 0$, which is determined by $\kappa_c^{(1)} = \kappa_c^{(2)} = q'/2$. Consequently, the infimum value of $\Lambda' = \alpha/\beta'$ would read

$$\Lambda'_{\text{inf}} = \frac{1}{p}\left(\frac{q'}{2}\right)^{1/p-1}\left(1-\frac{q}{2}\right)^{-1/p-1} \tag{24}$$

where q and q' were defined in advance.

Figure 10 depicts infimum and allowable ranges of $\Lambda = \alpha/\beta$ in terms of exponent p, normalized contractile density $\varsigma = \rho_0/E$ and normalized chemo-mechanical coupling parameter $\mathcal{B} = \beta E$. Since increasing exponent p as well as decreasing normalized contractile density ς and chemo-mechanical coupling parameter $\mathcal{B}$ would lower the upper-branch predicted motility level, only a choice of higher polarization parameter (reflected in normalized Λ) would make amends for the reduced cell contractility as demonstrated by Fig. 10.

Last, the infima (lower bounds) to both the normalized contractile density ς and chemo-mechanical coupling parameter $\mathcal{B}$ are set by the condition of nonnegativity of $\eta_c^{(2)}$ in (19), due to its emanation from $\kappa_c^{(2)}$, proving always lower than $\kappa_c^{(1)}$. Accordingly, the infimum ς and $\mathcal{B}$ would be determined by letting the denominator of $\eta_c^{(2)}$ vanish. That is, the $\kappa_c^{(2)}$ solution to

$${\kappa_c}^{q}\left(1-c\kappa_c\right)^{2-q} = \frac{1}{p\Lambda'} \tag{25}$$

would yield $\kappa_{\text{cmin}}^{(2)}$. On the other hand, from the $2\kappa_c^{(2)} = q' - \sqrt{\Delta}$ correlation in (19), one can easily verify the following infimum to the $\varsigma'\mathcal{B}'$ product:

$$(\varsigma'\mathcal{B}')_{\text{inf}} = \left(q' - \kappa_{\text{cmin}}^{(2)}\right) p\, \kappa_{\text{cmin}}^{(2)} \tag{26}$$

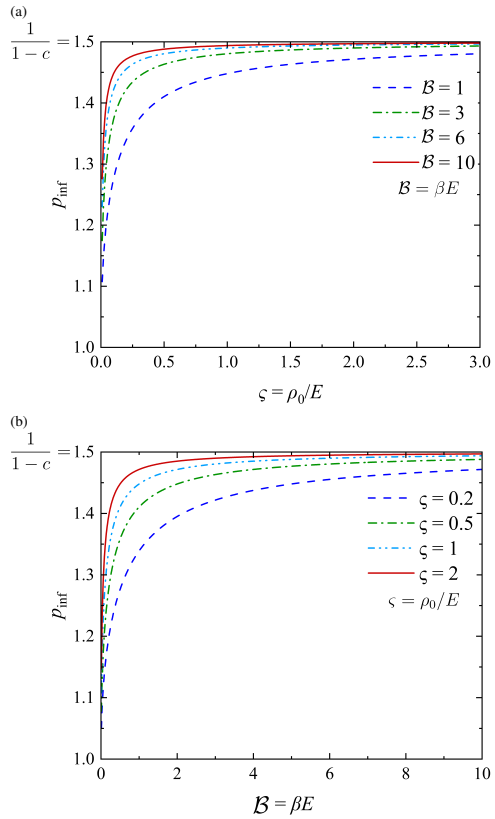

Figure 9: **Allowable range of model tuning power p.** Infimum values of model tuning power p: (a) in terms of normalized contractility density $\varsigma \equiv \rho_0/E$, (b) in terms of normalized chemo-mechanical coupling parameter $\mathcal{B} \equiv \beta E$. Cell parameters are identified by $E = 1.5$ kPa, $\nu = 0.27$, $(\varsigma, \mathcal{B}, \Lambda) = (0.2, 4.5, 1)$.

Note further that the sign of η_c in (19) is partly affected by the sign of $\mathcal{G}$. Hence, the positivity of $\mathcal{G}$ imparts an additional constraint on $\mathcal{B}$. In the case of a cell embedded in an infinite ECM, such constraint requires that $\mathcal{B} > \frac{1}{1-2\nu}$. Hence, infimum ς and $\mathcal{B}$ would be obtainable from the combination of Eq's (26) and (25) with the above additional constraint, which delivers

$$\begin{cases} \forall\mathcal{B}: \quad \varsigma_{\text{inf}} = \dfrac{\left(q'-\kappa_{\text{cmin}}^{(2)}\right)pc\,\kappa_{\text{cmin}}^{(2)}}{\mathcal{B}'} \\ \forall\varsigma: \quad \mathcal{B}'_{\text{inf}} = \min\left\{\dfrac{\left(q'-\kappa_{\text{cmin}}^{(2)}\right)pc\,\kappa_{\text{cmin}}^{(2)}}{\varsigma'}\,,\ \dfrac{1}{\Delta G(1-2\nu)}\right\} \end{cases} \tag{27}$$

All the same, the maximum allowable values for ς and $\mathcal{B}$ are derivable from the minimum value of the discriminant in (19), *i.e.* $\Delta = 0$. Therefore, the supremum (upper bound) value for ς and $\mathcal{B}$ would be obtained from the infimum value of the other.

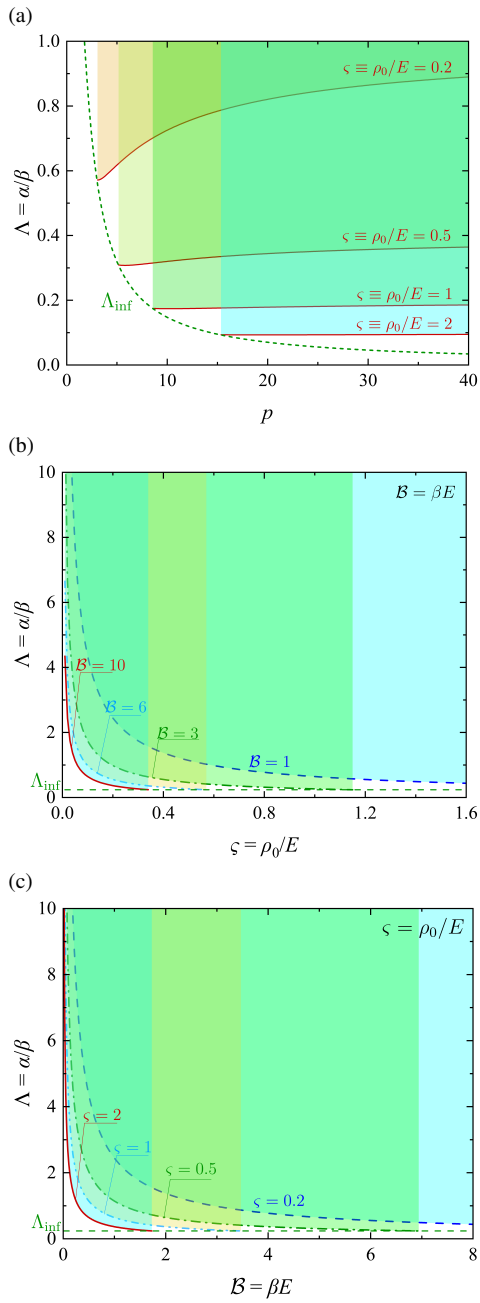

Figure 10: **Allowable range of stress polarization parameter.** Ranges of the normalized polarization parameter $\Lambda \equiv \alpha/\beta$ with its infimum value showing as lower bound: (a) vs. model tuning power p, (b) vs. normalized contractility density $\varsigma \equiv \rho_0/E$ (at select normalized chemo-mechanical coupling parameters $\mathcal{B} \equiv \beta E$), (c) vs. normalized chemo-mechanical coupling parameter $\mathcal{B} \equiv \beta E$ (at select normalized contractility densities $\varsigma \equiv \rho_0/E$).

That is

$$\begin{cases} \forall \mathcal{B}: & \varsigma_{\rm max} = \frac{p}{4c}\frac{q^2}{\mathcal{B}'} \;\therefore\; \varsigma_{\rm sup} = \frac{p}{4c}\frac{q^2}{\mathcal{B}'_{\rm inf}} \\ \forall \varsigma: & \mathcal{B}'_{\rm max} = \frac{p}{4c}\frac{q^2}{\varsigma} \;\therefore\; \mathcal{B}'_{\rm sup} = \frac{p}{4c}\frac{q^2}{\varsigma_{\rm inf}} \end{cases} \tag{28}$$

where $\mathcal{B}'_{\rm inf}$ and $\varsigma_{\rm inf}$ follow Eq. (27).

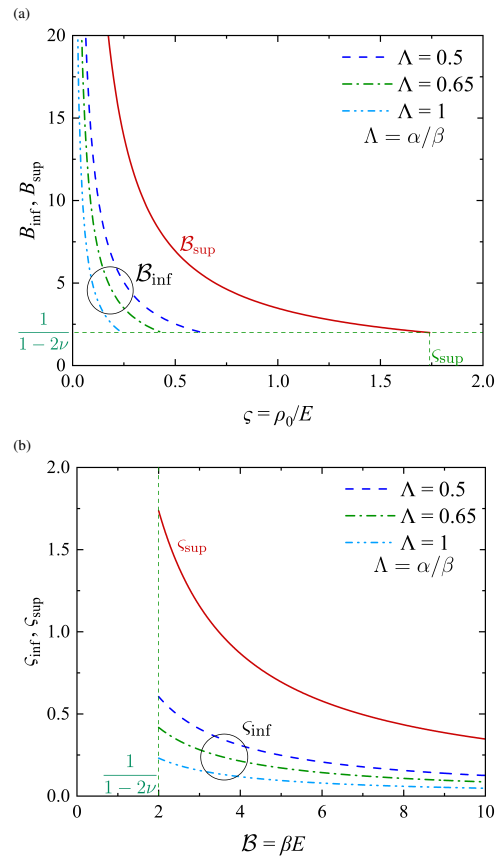

Figure 11: **Allowable ranges of contractile density and chemo-mechanical coupling.** Infimum and supremum values of normalized contractile density $\varsigma \equiv \rho_0/E$ and chemo-mechanical coupling parameter $\mathcal{B} \equiv \beta E$ at select values of normalized polarization parameters $\Lambda \equiv \alpha/\beta$. Cell parameters are identified by $E = 1.5$ kPa and $\nu = 0.27$. Model tuning parameters are also fixed at $(p, c) = (6, 1/3)$.

From Eq's (26)–(28), the dimensionless parameters $\mathcal{B}' = \beta' E$ and $\varsigma = \rho_0/E$ are found to be physical conjugates. That is, at a given steady state, one should decrease with the other. Note that, unlike ς' and ς that would differ in a c factor, $\mathcal{B}'$ and $\mathcal{B}$ can be considered equal without loss of generality inasmuch as ΔG, as primitively defined in (2), is merely a scaling factor that can easily get absorbed into β. Figure 11 shows example curves for allowable ranges of $\mathcal{B}$ and ς at various normalized polarization parameters Λ, each plotted vs. the other.

Once the above-discussed model parameters are defined, the bounds to trizonal solution can be evaluated in terms of the minimum and maximum critical stiffness ratios $\eta_{\rm c}^{(1)}$ and $\eta_{\rm c}^{(2)}$, as indicated by Fig. 12.

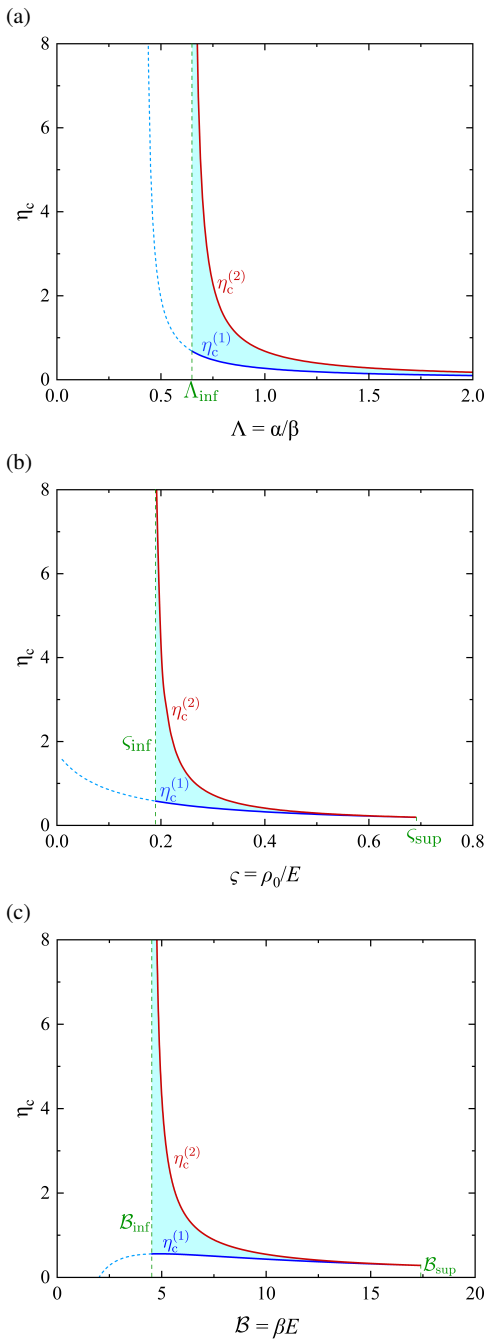

Figure 12: **Minimum and maximum critical stiffnesses for trizonal cell state.** Bounds to the stiffness overlapping interval $\eta_c^{(1)}$ and $\eta_c^{(2)}$: (a) in terms of the normalized polarization parameter $\Lambda \equiv \alpha/\beta$ (with $(\varsigma, \mathcal{B}) = (0.2, 4.5)$), (b) in terms of normalized contractile density $\varsigma \equiv \rho_0/E$ (with $\mathcal{B} = 4.5$), (c) in terms of the normalized chemo-mechanical coupling parameter $\mathcal{B} \equiv \beta E$ (with $\varsigma = 0.2$). Other cell parameters are identified by $E = 1.5$ kPa and $\nu = 0.27$. Model tuning parameters are also fixed at $(p, c) = (6, 1/3)$.

The lower value $\eta_c^{(1)}$ would then represent a measure of the minimum ECM stiffness that triggers shape transition, cell elongation and metastatic invasiveness. Besides, the upper value $\eta_c^{(2)}$ signifies the maximum ECM stiffness which generates two possible steady states of the cell, one non-invasive and one metastatic. Any value beyond $\eta_c^{(2)}$ would represent a fully invasive cell state. Nevertheless, cell elongation and invasiveness in such high ranges of ECM stiffness would decrease with increasing stiffness due to the highly dense, intertwined (basket-weave) network of fibers. Section 3.1 elaborates on this matter.

6 Acknowledgements

Authors genuinely acknowledge support from the National Science Foundation under grant No's 1953572, 1548571 and National Institute of Health under grant No. 6463801. Further acknowledgement goes to Prof. V. Shenoy, who initiated the idea of proposing a trizonal model and provided constructive feedback on model predictions. Last but not least, experimental support from Prof. P. Friedl (Department of Genitourinary Medical Oncology, Division of Cancer Medicine, MD Anderson Cancer Center) for provision of cell culture data, and technical support from Xingyu Chen (former PhD student, current machine learning engineer, recommendation and algorithm) for providing sketches of two-way feedback between cell and ECM.

References

[1] Thomas Lecuit and Pierre-Francois Lenne. Cell surface mechanics and the control of cell shape, tissue patterns and morphogenesis. *Nature reviews Molecular cell biology*, 8(8):633–644, 2007.

[2] Jos Käfer, Takashi Hayashi, Athanasius FM Marée, Richard W Carthew, and François Graner. Cell adhesion and cortex contractility determine cell patterning in the drosophila retina. *Proceedings of the National Academy of Sciences*, 104(47):18549–18554, 2007.

[3] Edouard Hannezo, Jacques Prost, and Jean-Francois Joanny. Theory of epithelial sheet morphology in three dimensions. *Proceedings of the National Academy of Sciences*, 111(1):27–32, 2014.

[4] Jiyeon Kim and Ralph J DeBerardinis. Mechanisms and implications of metabolic heterogeneity in cancer. *Cell metabolism*, 30(3):434–446, 2019.

[5] Xin Jin, Zelalem Demere, Karthik Nair, Ahmed Ali, Gino B Ferraro, Ted Natoli, Amy Deik, Lia Petronio, Andrew A Tang, Cong Zhu, et al. A metastasis map

of human cancer cell lines. *Nature*, 588(7837):331–336, 2020.

[6] Kevin Chen, Kivilcim Ozturk, Ryne L Contreras, Jessica Simon, Sean McCann, Wei Ji Chen, Hannah Carter, and Stephanie I Fraley. Phenotypically supervised single-cell sequencing parses within-cell-type heterogeneity. *Iscience*, 24(1):101991, 2021.

[7] Matthew R Zanotelli, Jian Zhang, Ismael Ortiz, Wenjun Wang, Neil C Chada, and Cynthia A Reinhart-King. Highly motile cells are metabolically responsive to collagen density. *Proceedings of the National Academy of Sciences*, 119(18):e2114672119, 2022.

[8] Jiri Zavadil, John Haley, Raghu Kalluri, Senthil K Muthuswamy, and Erik Thompson. Epithelial-mesenchymal transition, 2008.

[9] Raghu Kalluri, Robert A Weinberg, et al. The basics of epithelial-mesenchymal transition. *The Journal of clinical investigation*, 119(6):1420–1428, 2009.

[10] Douglas Hanahan and Robert A Weinberg. Hallmarks of cancer: the next generation. *cell*, 144(5):646–674, 2011.

[11] Dingcheng Gao, Linda T Vahdat, Stephen Wong, Jenny C Chang, and Vivek Mittal. Microenvironmental regulation of epithelial–mesenchymal transitions in cancerepithelial–mesenchymal transitions in metastasis. *Cancer research*, 72(19):4883–4889, 2012.

[12] William J Polacheck, Ioannis K Zervantonakis, and Roger D Kamm. Tumor cell migration in complex microenvironments. *Cellular and Molecular Life Sciences*, 70:1335–1356, 2013.

[13] Hideki Yamaguchi and John Condeelis. Regulation of the actin cytoskeleton in cancer cell migration and invasion. *Biochimica et Biophysica Acta (BBA)-Molecular Cell Research*, 1773(5):642–652, 2007.

[14] Kaoru Miyazaki, Jun Oyanagi, Daisuke Hoshino, Shinsaku Togo, Hiromichi Kumagai, and Yohei Miyagi. Cancer cell migration on elongate protrusions of fibroblasts in collagen matrix. *Scientific reports*, 9(1):292, 2019.

[15] David Caballero, Virginia Brancato, Ana C Lima, Catarina M Abreu, Nuno M Neves, Vitor M Correlo, Joaquim M Oliveira, Rui L Reis, and Subhas C Kundu. Tumor-associated protrusion fluctuations as a signature of cancer invasiveness. *Advanced Biology*, 5(9):2101019, 2021.

[16] Farid Alisafaei, Delaram Shakiba, Leanne Iannucci, Matthew Davidson, Kenneth Pryse, Pen-hsiu Grace Chao, Jason Burdick, Spencer Lake, Elliot Elson, Vivek Shenoy, et al. Tension anisotropy drives phenotypic transitions of cells via two-way cell-ecm feedback. *bioRxiv*, pages 2022–03, 2022.

[17] Ruggero Pardi et al. Signal transduction by adhesion receptors. In *Nature Education*, volume 3, pages 38–42. 2010.

[18] Sean P Palecek, Joseph C Loftus, Mark H Ginsberg, Douglas A Lauffenburger, and Alan F Horwitz. Integrin-ligand binding properties govern cell migration speed through cell-substratum adhesiveness. *Nature*, 385(6616):537–540, 1997.

[19] Joseph C Loftus, Robert C Liddington, et al. Cell adhesion in vascular biology. new insights into integrin-ligand interaction. *The Journal of clinical investigation*, 99(10):2302–2306, 1997.

[20] Benjamin Geiger, Alexander Bershadsky, Roumen Pankov, and Kenneth M Yamada. Transmembrane crosstalk between the extracellular matrix and the cytoskeleton. *Nature reviews Molecular cell biology*, 2(11):793–805, 2001.

[21] Nathalie Q Balaban, Ulrich S Schwarz, Daniel Riveline, Polina Goichberg, Gila Tzur, Ilana Sabanay, Diana Mahalu, Sam Safran, Alexander Bershadsky, Lia Addadi, et al. Force and focal adhesion assembly: a close relationship studied using elastic micropatterned substrates. *Nature cell biology*, 3(5):466–472, 2001.

[22] Claudia Tanja Mierke, Benjamin Frey, Martina Fellner, Martin Herrmann, and Ben Fabry. Integrin $\alpha 5\beta 1$ facilitates cancer cell invasion through enhanced contractile forces. *Journal of cell science*, 124(3):369–383, 2011.

[23] Evelyn B Voura, Ravi A Ramjeesingh, Anthony MP Montgomery, and Chi-Hung Siu. Involvement of integrin $\alpha \mathrm{v}\beta 3$and cell adhesion molecule l1 in transendothelial migration of melanoma cells. *Molecular biology of the cell*, 12(9):2699–2710, 2001.

[24] Uwe H Frixen, Jfirgen Behrens, Martin Sachs, Gertrud Eberle, Beate Voss, Angelika Warda, Dorothea Löchner, and Walter Birchmeier. E-cadherin-mediated cell-cell adhesion prevents invasiveness of human carcinoma cells. *The Journal of cell biology*, 113(1):173–185, 1991.

[25] Feng Qian, Zi-Chao Zhang, Xue-Feng Wu, Yu-Pei Li, and Qiang Xu. Interaction between integrin $\alpha 5$ and fibronectin is required for metastasis of b16f10 melanoma cells. *Biochemical and biophysical research communications*, 333(4):1269–1275, 2005.

[26] Heng Wu, Yu-Long Liang, Zengxia Li, Jiawei Jin, Wen Zhang, Lingling Duan, and Xiliang Zha. Positive expression of e-cadherin suppresses cell adhesion to fibronectin via reduction of $\alpha 5\beta 1$ integrin in human breast carcinoma cells. *Journal of cancer research and clinical oncology*, 132:795–803, 2006.

[27] Patrick T Caswell, Heather J Spence, Maddy Parsons, Dominic P White, Katherine Clark, Kwai Wa Cheng, Gordon B Mills, Martin J Humphries, Anthea J Messent, Kurt I Anderson, et al. Rab25 associates with $\alpha 5\beta 1$ integrin to promote invasive migration in 3d microenvironments. *Developmental cell*, 13(4):496–510, 2007.

[28] Patrick T Caswell, May Chan, Andrew J Lindsay, Mary W McCaffrey, David Boettiger, and Jim C Norman. Rab-coupling protein coordinates recycling of $\alpha 5\beta 1$ integrin and egfr1 to promote cell migration in 3d microenvironments. *The Journal of cell biology*, 183(1):143–155, 2008.

[29] Kenjiro Sawada, Anirban K Mitra, A Reza Radjabi, Vinay Bhaskar, Emily O Kistner, Maria Tretiakova, Sujatha Jagadeeswaran, Anthony Montag, Amy Becker, Hilary A Kenny, et al. Loss of e-cadherin promotes ovarian cancer metastasis via $\alpha 5$-integrin, which is a therapeutic target. *Cancer research*, 68(7):2329–2339, 2008.

[30] Gerhard Fritz, Ingo Just, and Bernd Kaina. Rho gtpases are over-expressed in human tumors. *International journal of cancer*, 81(5):682–687, 1999.

[31] Matthew J Paszek, Nastaran Zahir, Kandice R Johnson, Johnathon N Lakins, Gabriela I Rozenberg, Amit Gefen, Cynthia A Reinhart-King, Susan S Margulies, Micah Dembo, David Boettiger, et al. Tensional homeostasis and the malignant phenotype. *Cancer cell*, 8(3):241–254, 2005.

[32] Muhammad H Zaman, Linda M Trapani, Alisha L Sieminski, Drew MacKellar, Haiyan Gong, Roger D Kamm, Alan Wells, Douglas A Lauffenburger, and Paul Matsudaira. Migration of tumor cells in 3d matrices is governed by matrix stiffness along with cell-matrix adhesion and proteolysis. *Proceedings of the National Academy of Sciences*, 103(29):10889–10894, 2006.

[33] Vivek B Shenoy, Hailong Wang, and Xiao Wang. A chemo-mechanical free-energy-based approach to model durotaxis and extracellular stiffness-dependent contraction and polarization of cells. *Interface focus*, 6(1):20150067, 2016.

[34] Matthew R Zanotelli, Zachary E Goldblatt, Joseph P Miller, Francois Bordeleau, Jiahe Li, Jacob A VanderBurgh, Marsha C Lampi, Michael R King, and Cynthia A Reinhart-King. Regulation of atp utilization during metastatic cell migration by collagen architecture. *Molecular biology of the cell*, 29(1):1–9, 2018.

[35] B. C. Isenberg, P. A. DiMilla, M. Walker, S. Kim, and J. Y. Wong. Vascular smooth muscle cell durotaxis depends on substrate stiffness gradient strength. *Biophysical journal*, 97(5):1313–1322, 2009.

[36] Jingchen Feng, Herbert Levine, Xiaoming Mao, and Leonard M Sander. Cell motility, contact guidance, and durotaxis. *Soft matter*, 15(24):4856–4864, 2019.

[37] Jaime A Espina, Cristian L Marchant, and Elias H Barriga. Durotaxis: the mechanical control of directed cell migration. *The FEBS journal*, 289(10):2736–2754, 2022.

[38] Hossein Ahmadzadeh, Marie R Webster, Reeti Behera, Angela M Jimenez Valencia, Denis Wirtz, Ashani T Weeraratna, and Vivek B Shenoy. Modeling the two-way feedback between contractility and matrix realignment reveals a nonlinear mode of cancer cell invasion. *Proceedings of the National Academy of Sciences*, 114(9):E1617–E1626, 2017.

[39] Amanpreet Kaur, Brett L Ecker, Stephen M Douglass, Curtis H Kugel III, Marie R Webster, Filipe V Almeida, Rajasekharan Somasundaram, James Hayden, Ehsan Ban, Hossein Ahmadzadeh, et al. Remodeling of the collagen matrix in aging skin promotes melanoma metastasis and affects immune cell motility. *Cancer discovery*, 9(1):64–81, 2019.

[40] Yusheng Wu, Matthew R Zanotelli, Jian Zhang, and Cynthia A Reinhart-King. Matrix-driven changes in metabolism support cytoskeletal activity to promote cell migration. *Biophysical Journal*, 120(9):1705–1717, 2021.

[41] François Berthod, Lucie Germain, Hui Li, Wen Xu, Odile Damour, and François A Auger. Collagen fibril network and elastic system remodeling in a reconstructed skin transplanted on nude mice. *Matrix Biology*, 20(7):463–473, 2001.

[42] Regina Weinmüllner, Barbara Zbiral, Adnan Becirovic, Elena Maria Stelzer, Fabian Nagelreiter, Markus Schosserer, Ingo Lämmermann, Lisa Liendl, Magdalena Lang, Lucia Terlecki-Zaniewicz, et al. Organotypic human skin culture models constructed with senescent fibroblasts show hallmarks of skin aging. *npj Aging and Mechanisms of Disease*, 6(1):4, 2020.

[43] Eva Roig-Rosello and Patricia Rousselle. The human epidermal basement membrane: a shaped and cell instructive platform that aging slowly alters. *Biomolecules*, 10(12):1607, 2020.

[44] Pei-Hsun Wu, Anjil Giri, Sean X Sun, and Denis Wirtz. Three-dimensional cell migration does not follow a random walk. *Proceedings of the National Academy of Sciences*, 111(11):3949–3954, 2014.

[45] Hailong Wang, AS Abhilash, Christopher S Chen, Rebecca G Wells, and Vivek B Shenoy. Long-range force transmission in fibrous matrices enabled by tension-driven alignment of fibers. *Biophysical journal*, 107(11):2592–2603, 2014.

[46] Stephanie I Fraley, Pei-hsun Wu, Lijuan He, Yunfeng Feng, Ranjini Krisnamurthy, Gregory D Longmore, and Denis Wirtz. Three-dimensional matrix fiber alignment modulates cell migration and mt1-mmp utility by spatially and temporally directing protrusions. *Scientific reports*, 5(1):1–13, 2015.

[47] Bo Ri Seo, Xingyu Chen, Lu Ling, Young Hye Song, Adrian A Shimpi, Siyoung Choi, Jacqueline Gonzalez, Jiranuwat Sapudom, Karin Wang, Roberto Carlos Andresen Eguiluz, et al. Collagen microarchitecture mechanically controls myofibroblast differentiation. *Proceedings of the National Academy of Sciences*, 117(21):11387–11398, 2020.

[48] Arja Ray, Oscar Lee, Zaw Win, Rachel M Edwards, Patrick W Alford, Deok-Ho Kim, and Paolo P Provenzano. Anisotropic forces from spatially constrained focal adhesions mediate contact guidance directed cell migration. *Nature communications*, 8(1):14923, 2017.

[49] Farid Alisafaei, Doorgesh Sharma Jokhun, GV Shivashankar, and Vivek B Shenoy. Regulation of nuclear architecture, mechanics, and nucleocytoplasmic shuttling of epigenetic factors by cell geometric constraints. *Proceedings of the National Academy of Sciences*, 116(27):13200–13209, 2019.

[50] Mark J Mondrinos, Farid Alisafaei, Alex Y Yi, Hossein Ahmadzadeh, Insu Lee, Cassidy Blundell, Jeongyun Seo, Matthew Osborn, Tae-Joon Jeon, Sun Min Kim, et al. Surface-directed engineering of tissue anisotropy in microphysiological models of musculoskeletal tissue. *Science Advances*, 7(11):eabe9446, 2021.

[51] K. Katoh, Y. Kano, M. Amano, H. Onishi, K. Kaibuchi, and K. Fujiwara. Rho-kinase–mediated contraction of isolated stress fibers. *The Journal of cell biology*, 153(3):569–584, 2001.

[52] M. J. Tyska and D. M. Warshaw. The myosin power stroke. *Cell motility and the cytoskeleton*, 51(1):1–15, 2002.

[53] J. Étienne, J. Fouchard, D. Mitrossilis, N. Bufi, P. Durand-Smet, and A. Asnacios. Cells as liquid motors: Mechanosensitivity emerges from collective dynamics of actomyosin cortex. *Proceedings of the National Academy of Sciences*, 112(9):2740–2745, 2015.

[54] M. Honjo, H. Tanihara, M. Inatani, N. Kido, T. Sawamura, B. YJT Yue, S. Narumiya, and Y. Honda. Effects of rho-associated protein kinase inhibitor y-27632 on intraocular pressure and outflow facility. *Investigative ophthalmology & visual science*, 42(1):137–144, 2001.

[55] Y. Sawada, M. Tamada, B. J. Dubin-Thaler, O. Cherniavskaya, R. Sakai, S. Tanaka, and M. P. Sheetz. Force sensing by mechanical extension of the src family kinase substrate p130cas. *Cell*, 127(5):1015–1026, 2006.

[56] S. Pellegrin and H. Mellor. Actin stress fibres. *Journal of cell science*, 120(20):3491–3499, 2007.

[57] E. Puklin-Faucher and M. P. Sheetz. The mechanical integrin cycle. *Journal of cell science*, 122(2):179–186, 2009.

[58] B. D. Matthews, C. K. Thodeti, J. D. Tytell, A. Mammoto, D. R. Overby, and D. E. Ingber. Ultra-rapid activation of trpv4 ion channels by mechanical forces applied to cell surface $\beta 1$ integrins. *Integrative Biology*, 2(9):435–442, 2010.

[59] J. Steinwachs, C. Metzner, K. Skodzek, N. Lang, I. Thievessen, C. Mark, S. Münster, K. E. Aifantis, and B. Fabry. Three-dimensional force microscopy of cells in biopolymer networks. *Nature methods*, 13(2):171–176, 2016.

[60] D. Mitrossilis, J. Fouchard, D. Pereira, F. Postic, A. Richert, M. Saint-Jean, and A. Asnacios. Real-time single-cell response to stiffness. *Proceedings of the national academy of sciences*, 107(38):16518–16523, 2010.

[61] J. S. Park, C. J. Burckhardt, R. Lazcano, L. M. Solis, T. Isogai, L. Li, C. S. Chen, B. Gao, J. D. Minna, R. Bachoo, et al. Mechanical regulation of glycolysis via cytoskeleton architecture. *Nature*, 578(7796):621–626, 2020.

[62] K. P. Mishra. Cell membrane oxidative damage induced by gamma-radiation and apoptotic sensitivity. *Journal of environmental pathology, toxicology and oncology*, 23(1), 2004.

[63] F. M. Campos, J. A. Couto, A. R. Figueiredo, I. V. Tóth, A. O. Rangel, and T. A. Hogg. Cell membrane damage induced by phenolic acids on wine lactic acid bacteria. *International journal of food microbiology*, 135(2):144–151, 2009.

[64] H. L. Karlsson, P. Cronholm, Y. Hedberg, M. Tornberg, L. De Battice, S. Svedhem, and I. O. Wallinder. Cell membrane damage and protein interaction induced by copper containing nanoparticles—importance of the metal release process. *Toxicology*, 313(1):59–69, 2013.

[65] Katarina Wolf, Mariska Te Lindert, Marina Krause, Stephanie Alexander, Joost Te Riet, Amanda L Willis, Robert M Hoffman, Carl G Figdor, Stephen J Weiss, and Peter Friedl. Physical limits of cell migration: control by ecm space and nuclear deformation and tuning by proteolysis and traction force. *Journal of Cell Biology*, 201(7):1069–1084, 2013.

[66] M. Radmacher, M. Fritz, and P. K. Hansma. Imaging soft samples with the atomic force microscope: gelatin in water and propanol. *Biophysical journal*, 69(1):264–270, 1995.

[67] A. J. Engler, L. Richert, J. Y. Wong, C. Picart, and D. E. Discher. Surface probe measurements of the elasticity of sectioned tissue, thin gels and polyelectrolyte multilayer films: correlations between substrate stiffness and cell adhesion. *Surface science*, 570(1-2):142–154, 2004.

[68] A. J. Engler, F. Rehfeldt, S. Sen, and D. E. Discher. Microtissue elasticity: measurements by atomic force microscopy and its influence on cell differentiation. *Methods in cell biology*, 83:521–545, 2007.

[69] T. G. Kuznetsova, M. N. Starodubtseva, N. I. Yegorenkov, S. A. Chizhik, and R. I. Zhdanov. Atomic force microscopy probing of cell elasticity. *Micron*, 38(8):824–833, 2007.

[70] D. O. Velez, S. K. Ranamukhaarachchi, A. Kumar, R. N. Modi, E. W Lim, A. J. Engler, C. M. Metallo, and S. I. Fraley. 3d collagen architecture regulates cell adhesion through degradability, thereby controlling metabolic and oxidative stress. *Integrative Biology*, 11(5):221–234, 2019.

[71] J. N. Goodier and S. Timoshenko. *Theory of elasticity*. McGraw-Hill, 1970.

[72] O. Langholz, D. Röckel, C. Mauch, E. Kozlowska, I. Bank, T. Krieg, and B. Eckes. Collagen and collagenase gene expression in three-dimensional collagen lattices are differentially regulated by alpha 1 beta 1 and alpha 2 beta 1 integrins. *The Journal of cell biology*, 131(6):1903–1915, 1995.

[73] K. Wolf, Y. I. Wu, Y. Liu, J. Geiger, E. Tam, C. Overall, M. S. Stack, and P. Friedl. Multi-step pericellular proteolysis controls the transition from individual to collective cancer cell invasion. *Nature cell biology*, 9(8):893–904, 2007.

[74] R. Castelló-Cros, D. R. Khan, J. Simons, M. Valianou, and E. Cukierman. Staged stromal extracellular 3d matrices differentially regulate breast cancer cell responses through pi3k and beta1-integrins. *BMC cancer*, 9(1):1–19, 2009.

[75] I. Thievessen, N. Fakhri, J. Steinwachs, V. Kraus, R. S. McIsaac, L. Gao, B-C. Chen, M. A. Baird, M. W. Davidson, E. Betzig, et al. Vinculin is required for cell polarization, migration, and extracellular matrix remodeling in 3d collagen. *The FASEB Journal*, 29(11):4555, 2015.

[76] S. B. Anderson, C-C. Lin, D. V. Kuntzler, and K. S. Anseth. The performance of human mesenchymal stem cells encapsulated in cell-degradable polymer-peptide hydrogels. *Biomaterials*, 32(14):3564–3574, 2011.

[77] S. V. Plotnikov and C. M. Waterman. Guiding cell migration by tugging. *Current opinion in cell biology*, 25(5):619–626, 2013.

[78] R. Sunyer, V. Conte, J. Escribano, A. Elosegui-Artola, A. Labernadie, L. Valon, D. Navajas, J. M. García-Aznar, J. J. Muñoz, P. Roca-Cusachs, et al. Collective cell durotaxis emerges from long-range intercellular force transmission. *Science*, 353(6304):1157–1161, 2016.

[79] A. F. Bower. *Applied mechanics of solids*. CRC press, 2009.